RESEARCH ARTICLE | DECEMBER 15 2025

Efficient and flexible adaptive particle refinement for free-surface flows based on the regularized high-order diffusive smoothed particle hydrodynamics scheme

J. Michel ; G. Oger ; D. Le Touzé ; A. Colagrossi ; S. Marrone

Physics of Fluids 37, 122128 (2025)
https://doi.org/10.1063/5.0302483

Physics of Fluids ARTICLE pubs.aip.org/aip/pof

Efficient and flexible adaptive particle refinement for free-surface flows based on the regularized high-order diffusive smoothed particle hydrodynamics scheme

Cite as: Phys. Fluids **37**, 122128 (2025); doi: 10.1063/5.0302483
Submitted: 15 September 2025 · Accepted: 19 November 2025 ·
Published Online: 15 December 2025

J. Michel,[1] G. Oger,[1] D. Le Touzé,[1] A. Colagrossi,[2] and S. Marrone[2,a)]

AFFILIATIONS

[1]Nantes Université, École Centrale Nantes, CNRS, LHEEA, UMR 6598, F-44000 Nantes, France
[2]Institute of Marine Engineering (INM), National Research Council (CNR), Rome, Italy

[a)]**Author to whom correspondence should be addressed:** salvatore.marrone@cnr.it

ABSTRACT

The aim of the present work is the investigation of an adaptive particle refinement (APR) approach that enables large variations in particle size even in the presence of a free surface. In the smoothed particle hydrodynamics (SPH) literature, the existing APR or similar multi-resolution techniques can be categorized into three main approaches, essentially driven by the discrete differential operators selected. When a conservative formulation is retained, either variable smoothing-length techniques or buffer regions are generally employed. By contrast, in formulations using accurate but non-conservative SPH operators, large variations of the particle size are achievable without requesting any specific treatment. However, because of the difficulties of such formulations in addressing the free surface, they have so far been restricted to internal flows. Recently, a regularized high-order diffusive (RHOD)-SPH approach has been derived in the context of single resolution. In this approach an accurate formulation is used inside the bulk of the fluid, whereas a conservative one is preferred in the free-surface region. In the present paper, the ingredients required in the RHOD-SPH approach are extended to APR. Specifically, the Riemann-based diffusive terms and particle shifting technique are generalized to deal with particles of different sizes. A particle-splitting procedure is employed to enlarge the range of applications of the approach. The formulation is validated on six different test cases, with comparisons to both single-resolution and reference results.

I. INTRODUCTION

The smoothed particle hydrodynamics (SPH) method is a numerical method that has recently gained significant popularity as a numerical technique in engineering and, in particular, for fluid mechanics.[24,73,89] SPH is particularly advantageous in engineering applications where interfaces are subjected to large deformations, such as violent free-surface or multiphase flows.[39] However, while adaptive mesh refinement has been extensively developed for decades in other well-established numerical methods such as finite differences,[5] finite elements,[48] and finite volumes[19] and is now widely adopted[31] the SPH method still lacks a standard adaptive particle refinement (APR) technique to concentrate computational effort in specific regions of interest.[84] To overcome some of the SPH limitations, some researchers tried hybrid Lagrangian and Eulerian approaches, as in Ref. 66. Most of the APR techniques have been proposed within the framework of the weakly compressible approximation. Some examples of multi-resolution have been proposed also for incompressible particle methods, for instance, in fluid–structure interaction (FSI) schemes[33,34] and in the context of moving particle semi-implicit.[45,74,82]

Since the pioneering works in Refs. 22, 37, and 62, dozens of different techniques have been proposed during the last decade in the SPH literature. However, difficulties arise from both the Lagrangian and meshless characteristics of the method. On the one hand, the meshless spatial operators have to be chosen carefully to account for variable spatial resolution; on the other hand, specific techniques and criteria are required to handle the splitting of Lagrangian particles. Most of the APR or similar multi-resolution techniques in SPH can be categorized into three main approaches, essentially based on the

selected SPH operators and on the type of multi-resolution technique adopted. These different strategies are detailed in Sec. II to contextualize the present work within the existing literature on the topic.

In SPH modeling of free-surface flows, conservative spatial operators are generally preferred thanks to the inherent fulfillment of the dynamic boundary condition, as demonstrated in Ref. 15. In this context sharp variations of the particle size are difficult to handle, since it requires either variable smoothing-length operators[22] or the use of buffer regions.[13] Additionally, the use of conservative operators also entails potential limitations in terms of code implementation and parallel efficiency (see Refs. 21 and 28 and Sec. II). By contrast, accurate but non-conservative operators have been employed in Refs. 30 and 35, allowing sharp variations of the particle size without additional specific treatments. However, the applications of the latter formulations were restricted to internal flows.

Recently in Ref. 54, an SPH formulation has been derived featuring an accurate but non-conservative pressure gradient operator inside the fluid domain and a conservative one in the free-surface region. It was made possible thanks to the use of a particle shifting technique (PST) within a quasi-Lagrangian formulation, which allows the particle distribution to remain regular. Numerical diffusion was needed to reduce the occurrence of spurious high-frequency noise, and it was obtained by means of a Riemann solver. This formulation [called hereinafter regularized high-order diffusive (RHOD)-SPH] has been validated for both internal and free-surface flows, achieving a higher order of convergence than standard schemes with negligible conservation errors. Nevertheless, this approach was restricted to single-resolution cases only.

In the present work, we propose to combine the RHOD-SPH approach with the APR technique adopted in Refs. 30 and 35 in order to extend the latter to two-dimensional (2D) free-surface flows. To this purpose, the adopted Riemann solver is generalized to variable resolution, and an adaptation of the PST is introduced. To extend the range of applications, a particle-splitting procedure is used. Since no buffer regions are needed within this framework, the latter is not limited to specific predefined regions, but it is dynamically performed on the basis of different criteria, such as the distance to interfaces. As for particle coalescing, it is not addressed in the present work and will be treated in future works.

The paper is organized as follows: Sec. II is dedicated to the description of the current state of the art of APR in the SPH method. After a brief recall of the governing equations in Sec. III, the extension to APR of the RHOD-SPH approach is presented in Sec. IV with particular focus on the generalization of Riemann-based diffusive terms and PST. In Sec. V, the adopted particle-splitting technique is described. Finally, a discussion on the numerical results is provided in Sec. VI where six benchmarks are studied. Conclusions wrap up the paper.

II. STATE OF THE ART OF ADAPTIVE PARTICLE REFINEMENT IN THE SPH METHOD FOR ENGINEERING APPLICATIONS

A. Major APR techniques

Adaptivity and particle refinement are important topics of the current research on the SPH method. As a matter of fact, "Adaptivity" is one of the five grand challenges established by the SPH rEsearch and engineeRing International Community (SPHERIC).[84] The adaptive particle refinement techniques developed in the SPH method first appeared in the astrophysical context[4,28,36,60] where variable smoothing-length schemes were derived. In the engineering context, most of the current literature on the topic is based on some pioneering works. These works start from the variational approach proposed by Bonet and Lok[7] and extend it to the variable smoothing-length context as in Oger *et al.*[62]

More specifically, Lastiwka *et al.*[37] presented a 1D study of SPH operators when particles of different sizes are involved; Oger *et al.*[62] applied a variable smoothing-length scheme to 2D water entry. Finally, the work by Feldman and Bonet[22] is considered the first in the engineering context in which a dynamic particle refinement procedure is proposed and applied to free-surface flows. Most of the recent SPH schemes in the APR context are derived from the approach originally proposed in Ref. 22. It is worth noting that Vila[88] proposed a variable smoothing-length approach within an Arbitrary Lagrangian–Eulerian (ALE) framework, which has many similarities with the operators proposed in Ref. 22. The only application of that scheme, to the authors' knowledge, appeared in a conference article.[72]

Over the past two decades, numerous studies have been published on APR techniques. They are classified into three main approaches in the following and listed in Table I, where the main features are schematically outlined. Note that many names were used to call these adaptative particle refinement techniques, such as "dynamic refinement," "adaptive meshless," "adaptive resolution," "multi-resolution," "variable resolution," or even "multiscale."

Approach n.1: Conservative scheme with mixed interactions
A momentum-conservative formulation is adopted even when particles of different sizes interact, as in Ref. 22. To this purpose, the

TABLE I. Summary of the main works on APR techniques (called with different names) for engineering applications in the SPH literature; the present work is added for ease of comprehension. The different approaches are described in Sec. II A. "geom. splitting" refers to particle-splitting techniques based on predefined (generally circular or rectangular) geometrical domains, whereas "dyn. splitting" stands for a refinement based on other criteria (see Sec. II B for details). A specific denomination is used for Ref. 71, where the particles are generated in geometrical domains from mass fluxes.

	Approach	Particles creation	Fluid interfaces
Oger *et al.*[62]	1	No	Free surface
Feldman and Bonet[22]	1	geom. splitting	Free surface
Vacondio *et al.*[85]	1	dyn. splitting	No
Bian *et al.*[6]	2	geom. splitting	No
Khorasanizade and Sousa[35]	3	dyn. splitting	No
Hu *et al.*[30]	3	geom. splitting	No
Chiron *et al.*[13]	2	geom. splitting	Free surface
Yang and Kong[96]	1	dyn. splitting	Multiphase
Yang *et al.*[97]	1	dyn. splitting	Free surface
Muta and Ramachandran[59]	1	dyn. splitting	No
Ricci *et al.*[71]	2	geom. generation	Free surface
Present work	3	dyn. splitting	Free surface

SPH operators have to be modified accordingly, and additional terms accounting for the smoothing-length variations are formally involved. To limit the influence of these terms, one solution is to keep the spatial variations of the particle size, Δx, small (as in Refs. 62 and 96). Otherwise, if large variations of Δx are involved, the ratio $h/\Delta x$ (being h the smoothing length of the SPH interpolation kernel) is modified during particle splitting (or coalescing) in order to keep smooth the spatial variations of h. In particular, $h/\Delta x$ has to be significantly increased when the particle resolution is refined, as in the work by Vacondio *et al.*[85] In turn, the number of particle neighbors used in SPH operators largely increases, and so does the computational cost. This is a key aspect recurring in many other works.[11,29,59,69,96,97] It is also important to underline that the use of conservative operators along with variable smoothing length implies the adoption of a "scatter"-type implementation.[28] This can significantly deteriorate the computational efficiency, especially when GPU accelerators are used, as explained by Domínguez *et al.*[21] Note that, following Ref. 62, if the particle size variations are sufficiently small (size ratio between two adjacent particles below 3%), the ratio $h/\Delta x$ can be kept constant with negligible errors.

Approach n.2: Conservative scheme with buffer regions

In order to overcome the limitations of Approach n.1, other researchers[3,6,13,71] proposed a domain decomposition strategy in which the numerical domain is subdivided into subdomains, which can possibly move or track specific objects.[13,71] Each subdomain is characterized by a different particle size, and particles within have the same size. The ratio $h/\Delta x$ is constant throughout the numerical domain. The different subdomains communicate with each other by means of suitable buffer regions. This paradigm proved to be very efficient and robust and was successfully applied to a number of different problems.[23,47,78,93,101] However, the subdivision into different subdomains makes this type of APR less flexible with respect to schemes featuring mixed interactions. Additionally, specific treatments are required to handle the buffer regions, thus implying algorithm complexity.

Approach n.3: Non-conservative scheme with mixed interactions

A third approach is the one firstly presented by Khorasanizade and Sousa[35] and Hu *et al.*[30] In this case, more accurate SPH operators are adopted in the momentum equation. This choice enables direct interaction between particles of different sizes without the need to modify the ratio $h/\Delta x$ or apply specific treatments in the transition zones. This directly reflects on the possible "gather"-type of implementations (following the nomenclature in Ref. 28), which are beneficial for GPU codes.[21] The main drawback of this approach is that momenta are not formally conserved. To the authors' knowledge, this approach has been applied only to internal flows, due to difficulties of these non-conservative schemes to treat the free surface. The present work follows Approach n.3 and aims at extending it to free-surface flows, as highlighted in Table I.

Note that recently in the work by Ricci *et al.*,[70] an accurate but non-conservative pressure gradient was employed in Approach n.2. For other applications falling outside the scope of the present work, other specific APR techniques have been devised.[33,76,98]

B. Refinement procedures

As mentioned in Sec. II A, the first work addressing particle splitting is the one by Feldman and Bonet.[22] In that work triangular and hexagonal patterns were considered in two dimensions. Further, a method to determine the optimal smoothing length h and particle size Δx during the particle refinement procedure was presented. The hexagonal pattern was later used by Vacondio *et al.*[85] along with a suitable PST. The same pattern was adopted also by Muta and Ramachandran[59] and coupled to a coalescing technique in order to obtain a smooth transition of particle size. The optimization method introduced in Ref. 22 was extended by Reyes López *et al.*[69] for square refinement patterns. The latter was used also in Refs. 11 and 64, and it has become particularly popular in APR schemes adopting buffer regions.[13,71,78] Other refinement patterns were studied in Refs. 96 and 97. Furthermore, extensions to 3D were achieved using cubic patterns in Refs. 27 and 47 and icosahedron-shaped arrangements in Ref. 86.

Once a particle is split into child particles, physical quantities have to be assigned to these novel particles. In Ref. 22, the quantities were assigned to the child particles in order to ensure conservation of mass, momenta, and kinetic energy. This approach has become the standard one in particle splitting. Other researchers prefer accuracy with respect to conservation by employing a first-order interpolation of velocity and density, as in Ref. 30.

Finally, it is worth mentioning also the various refinement criteria employed in the literature. Most researchers adopt predefined geometrical (generally rectangular or circular) refinement zones.[13,22,30,69,71] More recently, refinement close to interfaces (solid boundaries, multiphase interfaces, and free surfaces) has been proposed, as in Refs. 59, 96, and 97. Other works adopted refinement criteria based on the fluid flow fields, such as the velocity, vorticity, or pressure fields.[25,35,41,69] Note that a refinement criterion based on the interpolation error was also proposed in Ref. 75.

III. GOVERNING EQUATIONS

The fluid is assumed to be a weakly compressible, Newtonian, isothermal, and barotropic medium. Under these hypotheses the governing equations are the Navier–Stokes equations

$$\frac{D\rho}{Dt} = -\rho\,\nabla\cdot\boldsymbol{u}, \quad \rho\frac{D\boldsymbol{u}}{Dt} = -\nabla P + \boldsymbol{F}^{\mu} + \rho\boldsymbol{f}, \quad \frac{D\boldsymbol{x}}{Dt} = \boldsymbol{u}, \tag{1}$$

where D/Dt represents the Lagrangian derivative, ρ the fluid density, P the fluid pressure, $\boldsymbol{u}$ the fluid velocity, $\boldsymbol{f}$ the external specific volume forces, $\boldsymbol{F}^{\mu}$ the viscous forces, and $\boldsymbol{x}$ the position of the considered material point. Since the fluid is barotropic, the pressure field and the density field are linked through an equation of state, which is linearized around a reference density value, ρ_0, due to the hypothesis of weak compressibility. The equation of state and the constraint derived from the latter condition read:

$$P = c_0^2(\rho - \rho_0), \quad c_0 \geq 10\max\left(\Delta U_{max}, \sqrt{\Delta P_{max}/\rho}\right), \tag{2}$$

where c_0 is the fluid sound speed. ΔU_{max} and ΔP_{max} are, respectively, the maximum velocity and pressure variations within the fluid domain.[50]

IV. GENERALIZATION OF THE RHOD-SPH SCHEME TO APR

In Ref. 54, the regularized high-order diffusive (RHOD)-SPH scheme has been presented. This scheme is based on four main elements:

(i) A particle shifting technique (PST) to maintain regular particle distributions[43] that lead to accurate interpolation of the SPH operators.[67]
(ii) A quasi-Lagrangian formulation to properly introduce this PST in the governing equations.[53,79]
(iii) Diffusive terms obtained by means of a Riemann solver.[65]
(iv) A switch on the pressure gradient approximation between a renormalized formulation in the bulk of the fluid and a conservative formulation in the free-surface region. The renormalized formulation inside the fluid allows us to avoid the Tensile Instability and to increase the order of accuracy of this operator.[20] The conservative formulation in the free-surface region allows us to fulfill the dynamic free-surface boundary condition.[15]

This RHOD-SPH scheme was developed in a single-resolution context, limiting its application to cases where the zones of interest follow the Lagrangian trajectories of the fluid flow. In the present section, its generalization to APR is presented, which is an extension to be able to handle particles with different size. The procedure used for the particle refinement itself is described in Sec. V.

Thus, the present section is dedicated to the derivation of the multi-resolution technique for a set of particles of different sizes. In Sec. IV A, the general framework is recalled. Then, the extension to multi-resolution requires the generalization of Riemann solvers, which is provided in Sec. IV B, and an extension of the PST, given in Sec. IV C. Thanks to these generalizations, particles of different sizes can be mixed and evolve together without the need for buffer regions or specific treatments, as described in Sec. IV D.

A. RHOD-SPH framework

Using the RHOD-SPH model described in Ref. 54, the Navier–Stokes equations for compressible flows (1) are discretized as follows:

$$\begin{cases} \dfrac{d\rho_i}{dt} = -\rho_i \langle \nabla \cdot \boldsymbol{u} \rangle_i - \rho_i \langle \nabla \cdot \boldsymbol{\delta u} \rangle_i + \langle \nabla \cdot (\rho \boldsymbol{\delta u}) \rangle_i + \Theta^{\rho}_{i,Rie}, \\ \rho_i \dfrac{d\boldsymbol{u}_i}{dt} = -\langle \nabla P \rangle_i + \rho_i \boldsymbol{f}_i + \langle \nabla \cdot (\rho\, \boldsymbol{u} \otimes \boldsymbol{\delta u}) \rangle_i + \boldsymbol{F}_i^{AD} \\ \qquad\qquad + \alpha^{\mu} \boldsymbol{F}_i^{\mu} + (1-\alpha^{\mu}) \boldsymbol{\Theta}^{\boldsymbol{u}}_{i,Rie}, \\ \dfrac{d\boldsymbol{x}_i}{dt} = \boldsymbol{u}_i + \boldsymbol{\delta u}_i, \quad V_i(t) = m_i / \rho_i(t), \quad P_i = c_0^2(\rho_i - \rho_0), \end{cases} \tag{3}$$

where subscript i refers to particle i. m_i is the mass of particle i and V_i its volume. $\boldsymbol{\delta u}$ is the particle shifting velocity used to regularize the particles' spatial distribution during their motion. In Sec. IV C, the specific law adopted in the present work is given. The time derivative d/dt used in Eq. (3) indicates a quasi-Lagrangian derivative, i.e.,

$$\frac{d(\bullet)}{dt} := \frac{\partial(\bullet)}{\partial t} + \nabla(\bullet) \cdot (\boldsymbol{u} + \boldsymbol{\delta u}) = \frac{D(\bullet)}{Dt} + \nabla(\bullet) \cdot \boldsymbol{\delta u}.$$

Since the magnitude of $\boldsymbol{\delta u}_i$ is small, the hypothesis of particle masses m_i being constant in time is valid.[1,79] The masses are initially set to $m_i = \rho_i(0)\, V_i(0)$ with $V_i(0)$ and $\rho_i(0)$ the initial particle volumes and densities. The spatial differential operators related to $\boldsymbol{\delta u}$ are discretized following Ref. 79 by

$$\begin{cases} \langle \nabla \cdot \boldsymbol{\delta u} \rangle_i = \sum_j (\boldsymbol{\delta u}_j - \boldsymbol{\delta u}_i) \cdot \nabla_i W_{ij} V_j, \\ \langle \nabla \cdot (\rho \boldsymbol{\delta u}) \rangle_i = \sum_j (\rho_i \boldsymbol{\delta u}_i + \rho_j \boldsymbol{\delta u}_j) \cdot \nabla_i W_{ij} V_j, \\ \langle \nabla \cdot (\rho\, \boldsymbol{u} \otimes \boldsymbol{\delta u}) \rangle_i = \sum_j (\rho_i \boldsymbol{u}_i \otimes \boldsymbol{\delta u}_i + \rho_j \boldsymbol{u}_j \otimes \boldsymbol{\delta u}_j) \nabla_i W_{ij} V_j, \end{cases} \tag{4}$$

where W is the $\mathcal{C}^2$-Wendland kernel function[92] adopted and subscript j indicates the neighboring particles to particle i. The notation $W_{ij} = W(||\boldsymbol{x}_j - \boldsymbol{x}_i||, R_i)$ is used and details about kernel radii R_i adopted with APR are given in Sec. IV D. The velocity divergence is expressed as

$$\langle \nabla \cdot \boldsymbol{u} \rangle_i = \sum_j (\boldsymbol{u}_j - \boldsymbol{u}_i) \cdot \nabla_i W_{ij} V_j. \tag{5}$$

As in Ref. 54, the pressure gradient approximation depends on the distance to the free surface (see also the left plot of Fig. 1). The free-surface detection algorithm by Marrone *et al.*[51] is used to detect the free-surface particles $\mathcal{F}$. The free-surface region is then defined as the union of $\mathcal{F}$ and $\mathcal{V}$, where the latter stands for vicinity particles, that is, particles having at least one free-surface particle within their kernel support, as sketched in the right plot of Fig. 1. Following Ref. 54, an additional criterion based on the Shepard values is added. It acts especially during free-surface reconnections where the free-surface detection algorithm can fail. In those circumstances particles may have a partially void kernel support without belonging to the free-surface region. Therefore, this criterion has been introduced for robustness purposes. The pressure gradient approximation reads

$$\langle \nabla P \rangle_i = \begin{cases} \mathbb{L}_i \sum_j (P_j - P_i) \nabla_i W_{ij} V_j & \text{if } i \in \mathcal{I} \text{ and } \Gamma_i \geq \Gamma_{th} \\ \sum_j (P_j + P_i) \nabla_i W_{ij} V_j & \text{otherwise,} \end{cases} \tag{6}$$

where Γ_i is the Shepard value defined as

$$\Gamma_i = \sum_j \Gamma_{ij}\,; \quad \Gamma_{ij} = W_{ij} V_j, \tag{7}$$

and Γ_{th} is a threshold value in this work set to $\Gamma_{th} = 0.85$, as a compromise between accuracy and robustness. $\mathbb{L}_i$ is the renormalization matrix[68]

$$\mathbb{L}_i = \left[\sum_j (\boldsymbol{x}_j - \boldsymbol{x}_i) \otimes \nabla_i W_{ij} V_j \right]^{-1}, \tag{8}$$

ensuring the exact gradient approximation of a linear pressure field. This property being valid for any particle distribution, it represents the key point of the present scheme with APR, as previously noted by Hu *et al.* in Ref. 30. Note that the choice of a non-symmetric formula for the pressure gradient entails the removal of the kernel function dependency on the smoothing length of neighboring particles. As already mentioned, this allows a "gather"-type implementation of the scheme, which has significant advantages when GPU acceleration is employed.[21] For the divergence operators $\langle \nabla \cdot (\rho \boldsymbol{\delta u}) \rangle_i$, $\langle \nabla \cdot (\rho\, \boldsymbol{u} \otimes \boldsymbol{\delta u}) \rangle_i$ and $\boldsymbol{F}_i^{AD}$ we preferred not to introduce an h-dependency, which would allow the symmetry of these operators to be preserved. With this choice we can maintain the "gather"-type implementation.

The acoustic damper term $\boldsymbol{F}_i^{AD}$ reads

$$\begin{aligned} \boldsymbol{F}_i^{AD} &= \alpha^{AD} \rho_0 c_0 h_i \sum_j (D_j + D_i) \nabla_i W_{ij} V_j; \\ D_k &= \sum_l (\boldsymbol{u}_l - \boldsymbol{u}_k) \cdot \nabla_k W_{kl} V_l, \end{aligned} \tag{9}$$

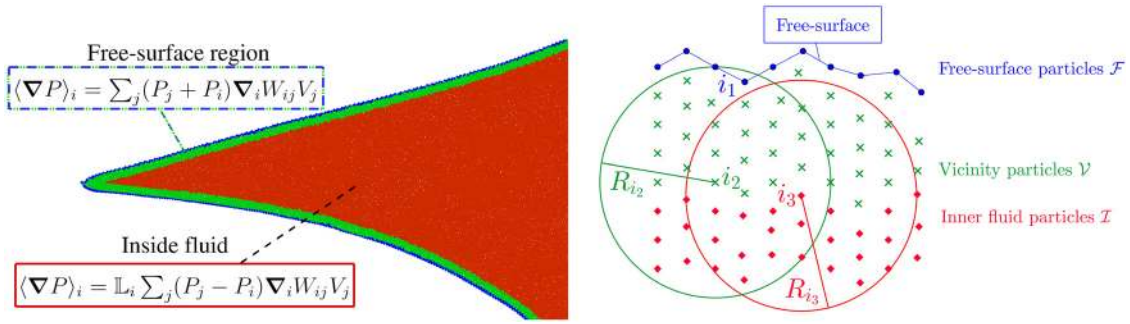

FIG. 1. Definition of the free-surface region and inner particles along with the related pressure gradient approximations as in Ref. 54. Left plot: pressure gradient approximations depending on the distance to the free surface, with $\mathbb{L}_i$ the renormalization matrix defined in Eq. (8). Right plot: sketch of the free-surface region defined as the union of free-surface particles $\mathcal{F}$ and vicinity particles $\mathcal{V}$ which are the particles having at least one free-surface particle within their kernel support. Inner particles $\mathcal{I}$ are particles that do not interact with free-surface particles. Free-surface particles are determined following Ref. 51. Reproduced with permission from Michel *et al.*, Phys. Fluids **35**(10), 103604 (2023). Copyright 2023 Authors, licensed under a Creative Commons Attribution License.

with ρ_0 the fluid density at rest, h_i the smoothing length associated with particle i, and $\alpha^{AD} = 1$ to allow the largest possible dissipation of the acoustic waves without affecting the time step.[81] $\boldsymbol{F}_i^{\mu}$ stands for the viscous forces, and the Monaghan and Gingold formulation[57] is used

$$\boldsymbol{F}_i^{\mu} = \mu \sum_j 2(d+2)\,\pi_{ij}\,\boldsymbol{\nabla}_i W_{ij} V_j, \quad \pi_{ij} = \frac{(\boldsymbol{u}_j - \boldsymbol{u}_i)\cdot(\boldsymbol{x}_j - \boldsymbol{x}_i)}{||\boldsymbol{x}_j - \boldsymbol{x}_i||^2}, \quad (10)$$

where μ is the dynamic viscosity coefficient and d is the spatial dimension. For studying low Reynolds numbers within the present framework, a higher-order Laplacian velocity operator, as in Refs. 2 and 30, could be used, provided its consistency is extended to viscous free-surface flows.

The symbols $\Theta^{\rho}_{i,Rie}$ and $\boldsymbol{\Theta}^{\boldsymbol{u}}_{i,Rie}$ in Eq. (3) denote the numerical diffusive terms stemming from the use of Riemann solvers, their derivation in the APR context being detailed in Sec. IV B [their expression is given in Eqs. (23) and (24), respectively]. $\alpha^{\mu} = \{1 \text{ if } \mu \neq 0\,;\, 0 \text{ otherwise}\}$ stands for a mutual exclusion term. Indeed, in the present work we remarked that considering $\boldsymbol{\Theta}^{\boldsymbol{u}}_{i,Rie}$ in addition to viscous forces $\boldsymbol{F}_i^{\mu}$ results in excessive dissipation. Therefore, when viscous flows are considered, the Riemann-based diffusive term in the momentum equation is disabled by setting $\alpha^{\mu} = 1$. This is analogous to what is commonly done when using δ-SPH formulations for simulating viscous flows.[80] Note that reducing the numerical viscosity induced by $\boldsymbol{\Theta}^{\boldsymbol{u}}_{i,Rie}$ in SPH represents an active research topic.[94,99]

Solid boundary conditions are modeled using mirrored ghost particles.[17,42] In Secs. VI C and VI F, the forces exerted by the fluid on solid bodies are used as a validation feature. In these cases, the forces are computed following Ref. 8. Finally, the scheme (3) is integrated in time by using a fourth-order Runge–Kutta scheme, and the following Courant–Friedrichs–Lewy numbers are adopted

$$\Delta t = \min_i \left(CFL_h \frac{R_i}{c_0}\,,\ \frac{CFL_h}{\alpha^{AD}} \frac{R_i}{c_0}\,,\ CFL_{\mu} \frac{\rho_0 R_i^2}{\mu} \right); \quad CFL_h = 0.5\,; \quad CFL_{\mu} = 0.025. \quad (11)$$

The time step constraints are dependent on the minimum particle size involved in the simulation without additional cost with respect to the uniform resolution scheme for the same level of discretization. Note that, for the Reynolds number range and coefficient α^{AD} adopted in the present work, the acoustic constraint is always the most restrictive.

B. Generalization of Riemann-based diffusive terms with APR

In Ref. 54, Riemann-based diffusive terms have been described for single resolution. Their extension to the APR context is derived in Secs. IV C 1–IV C 2. Before going into details about this extension, we briefly recall the main steps of the procedure for single resolution:

1. Considering a fictitious interface located at mid-distance between particles i and j, and determining the left and right states (ϕ_L and ϕ_R, respectively) at this fictitious interface using piecewise linear reconstructions and limitation.
2. Obtaining the Riemann problem solution $\boldsymbol{u}_E$ and P_E at this interface by using a Riemann solver.
3. Manipulating the velocity divergence and pressure gradient SPH approximations to make appear explicitly the values ϕ_{ij} obtained by a linear approximation at this interface; in Ref. 54, values corresponding to the arithmetic means $\frac{\boldsymbol{u}_i+\boldsymbol{u}_j}{2}$ and $\frac{P_i+P_j}{2}$ were chosen as initially proposed in Ref. 65. Replacing these values by the Riemann problem solution, thus giving the diffusive terms obtained by means of a Riemann solver.

When particles of different sizes are considered, the fictitious interface is not necessarily located at mid-distance between particles i and j (see Fig. 2), and the whole procedure has to be generalized, which is the aim of Subsections IV B 1–IV B 3.

1. Left and right states for the Riemann problem at the fictitious interface x_{ij}

With APR, as sketched in Fig. 2, the fictitious interface position $\boldsymbol{x}_{ij}$ between particles i and j located in $\boldsymbol{x}_i$ and $\boldsymbol{x}_j$ and of characteristic sizes Δx_i and Δx_j, respectively, is chosen as

$$\boldsymbol{x}_{ij} = \boldsymbol{x}_i + \omega_i(\boldsymbol{x}_j - \boldsymbol{x}_i) = \boldsymbol{x}_j + \omega_j(\boldsymbol{x}_i - \boldsymbol{x}_j), \quad \omega_i = \frac{\Delta x_i}{\Delta x_i + \Delta x_j}, \quad \omega_j = \frac{\Delta x_j}{\Delta x_i + \Delta x_j}, \quad (12)$$

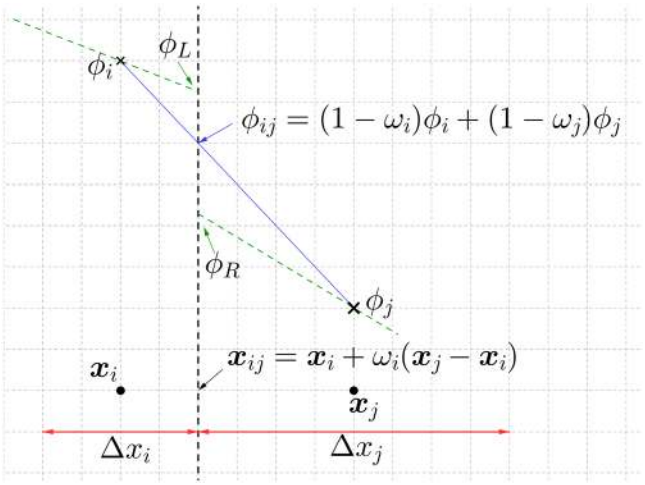

FIG. 2. Sketch of fictitious interface $\boldsymbol{x}_{ij}$ between particles i and j. Particle i (respectively j) is located in $\boldsymbol{x}_i$ (respectively $\boldsymbol{x}_j$), of characteristic size Δx_i (respectively Δx_j), of weight $\omega_i = \frac{\Delta x_i}{\Delta x_i + \Delta x_j}$ (respectively $\omega_j = \frac{\Delta x_j}{\Delta x_i + \Delta x_j}$) and of value ϕ_i (respectively ϕ_j). ϕ_L (respectively ϕ_R) represents the left state (respectively right state) obtained by reconstruction/limitation, while $\phi_{ij} = (1-\omega_i)\phi_i + (1-\omega_j)\phi_j$ stands for the linear interpolation of ϕ at position $\boldsymbol{x}_{ij}$.

where ω_i and ω_j are the weights of particles i and j, respectively. Note that by construction $\omega_i + \omega_j = 1$. For such a i–j interface located at $\boldsymbol{x}_{ij}$, the determination of the left state ϕ_L of the Riemann problem (see also Fig. 2) first consists in computing two slopes $\Delta\phi_i^1$ and $\Delta\phi_i^2$

$$\Delta\phi_i^1 = \frac{\phi_j - \phi_i}{||\boldsymbol{x}_j - \boldsymbol{x}_i||} \quad \text{and} \quad \Delta\phi_i^2 = \langle \nabla\phi \rangle_i^{\mathcal{L}} \cdot \boldsymbol{n}_{ij}, \tag{13}$$

with ϕ_i and ϕ_j the values of the field ϕ at $\boldsymbol{x}_i$ and $\boldsymbol{x}_j$, respectively, and where

$$\boldsymbol{n}_{ij} = \frac{\boldsymbol{x}_j - \boldsymbol{x}_i}{||\boldsymbol{x}_j - \boldsymbol{x}_i||} \quad \text{and} \quad \langle \nabla\phi \rangle_i^{\mathcal{L}} = \mathbb{L}_i \sum_j (\phi_j - \phi_i) \nabla_i W_{ij} V_j \tag{14}$$

with $\mathbb{L}_i$ defined in Eq. (8).

Then, as proposed in Refs. 58 and 87, the retained slope reads

$$\Delta\phi_i = \begin{cases} \dfrac{2\Delta\phi_i^1 \Delta\phi_i^2}{\Delta\phi_i^1 + \Delta\phi_i^2} & \text{if} \quad \Delta\phi_i^2 \Delta\phi_i^1 > 0 \\ 0 & \text{otherwise.} \end{cases} \tag{15}$$

Precisely, for slopes $\Delta\phi_i^1$ and $\Delta\phi_i^2$ of same sign, their harmonic mean is considered, while a constant reconstruction is employed otherwise. Finally, and following the same procedure for the right state, the left and right states are defined as

$$\begin{aligned} \phi_L &= \phi_i + \omega_i \Delta\phi_i ||\boldsymbol{x}_j - \boldsymbol{x}_i|| \\ \phi_R &= \phi_j + \omega_j \Delta\phi_j ||\boldsymbol{x}_i - \boldsymbol{x}_j||. \end{aligned} \tag{16}$$

2. The primitive variable Riemann solver

As in Refs. 53 and 54, the approximate Riemann solver, usually named primitive variable Riemann solver (PVRS)[83] is used, since it provides results that are very close to those predicted by the exact Riemann solver, but at a lower computational cost. The primitive variables being ρ and $\boldsymbol{u}$, the related pressure P is determined through Eq. (2). Since a constant speed of sound is imposed by Eq. (2), i.e., $c_L = c_R = c_0$, the Riemann problem solutions read

$$\boldsymbol{u}_E = \left[\frac{\rho_R u_R + \rho_L u_L}{\rho_R + \rho_L} + \frac{P_L - P_R}{c_0(\rho_L + \rho_R)} \right] \cdot \boldsymbol{n}_{ij}, \tag{17}$$

$$P_E = \frac{\rho_R P_L + \rho_L P_R}{\rho_R + \rho_L} + \frac{\rho_R \rho_L c_0 (u_L - u_R)}{\rho_R + \rho_L}. \tag{19}$$

3. Diffusive terms obtained by means of the Riemann solver

In order to express the diffusive terms obtained by means of the Riemann solver, it is first necessary to manipulate the velocity divergence and pressure gradient SPH operators to make appear explicitly the linear interpolation of the considered physical quantities ϕ at the interface $\boldsymbol{x}_{ij}$, i.e.,

$$\phi_{ij} = (1-\omega_i)\phi_i + (1-\omega_j)\phi_j, \tag{20}$$

as also sketched in Fig. 2. For the sake of brevity, the whole derivation is given for the diffusive term appearing in the continuity equation $\Theta^{\rho}_{i,Rie}$, a similar derivation enable to express $\boldsymbol{\Theta}^{\boldsymbol{u}}_{i,Rie}$.

To express $\Theta^{\rho}_{i,Rie}$, the first step consists in writing the velocity divergence (5) as

$$\begin{aligned} \langle \nabla \cdot \boldsymbol{u} \rangle_i &= \sum_j (\boldsymbol{u}_j - \boldsymbol{u}_i) \cdot \nabla_i W_{ij} V_j \\ &= \sum_j 2\left[(1-\omega_i)\boldsymbol{u}_i + (1-\omega_j)\boldsymbol{u}_j + \mathcal{R}_{ij} \right] \cdot \nabla_i W_{ij} V_j, \end{aligned} \tag{21}$$

with $\mathcal{R}_{ij}$ the remaining term equal to $\mathcal{R}_{ij} = -\left(\frac{3}{2} - \omega_i\right)\boldsymbol{u}_i - \left(\frac{1}{2} - \omega_j\right)\boldsymbol{u}_j$. Then, the Riemann diffusive term is introduced within the scheme by replacing the quantity $(1-\omega_i)\boldsymbol{u}_i + (1-\omega_j)\boldsymbol{u}_j$ in Eq. (21) by $\boldsymbol{u}_E$ the Riemann problem solution. It leads to

$$-\rho_i \langle \nabla \cdot \boldsymbol{u} \rangle_i + \Theta^{\rho}_{i,Rie} = -\rho_i \sum_j 2\left[\boldsymbol{u}_E + \mathcal{R}_{ij} \right] \cdot \nabla_i W_{ij} V_j, \tag{22}$$

and consequently $\Theta^{\rho}_{i,Rie}$ is expressed as

$$\begin{aligned} \Theta^{\rho}_{i,Rie} &= -\rho_i \sum_j 2\left[\boldsymbol{u}_E + \mathcal{R}_{ij} \right] \cdot \nabla_i W_{ij} V_j - \langle \nabla \cdot \boldsymbol{u} \rangle_i \\ &= -\rho_i \sum_j 2\left[\boldsymbol{u}_E + \mathcal{R}_{ij} - (1-\omega_i)\boldsymbol{u}_i \right. \\ &\quad \left. - (1-\omega_j)\boldsymbol{u}_j - \mathcal{R}_{ij} \right] \cdot \nabla_i W_{ij} V_j \\ &= -\rho_i \sum_j 2\left(\boldsymbol{u}_E - \left[(1-\omega_i)\boldsymbol{u}_i + (1-\omega_j)\boldsymbol{u}_j \right] \right) \cdot \nabla_i W_{ij} V_j. \end{aligned} \tag{23}$$

The diffusion term in the momentum equation $\boldsymbol{\Theta}^{\boldsymbol{u}}_{i,Rie}$ is derived using the same procedure and reads

$$\boldsymbol{\Theta}^{\boldsymbol{u}}_{i,Rie} = \begin{cases} -\mathbb{L}_i \sum_j \theta^{\boldsymbol{u}}_{ij} \boldsymbol{\nabla}_i W_{ij} V_j & \text{if } i \in \mathcal{I} \,\&\, \Gamma_i > 0.95 \\ -\sum_j \theta^{\boldsymbol{u}}_{ij} \boldsymbol{\nabla}_i W_{ij} V_j & \text{otherwise;} \end{cases} \qquad \theta^{\boldsymbol{u}}_{ij} = 2\left\{P_E - \left[(1-\omega_i)P_i + (1-\omega_j)P_j\right]\right\}. \tag{24}$$

Notably, for interactions between particles of the same size (i.e., with $\omega_i = \omega_j = \frac{1}{2}$) the Riemann-based diffusive terms derived in the present work are equivalent to those in Ref. 54. Note that Eq. (22) can be used for implementing the whole term $\langle \boldsymbol{\nabla} \cdot \boldsymbol{u} \rangle_i + \Theta^{\rho}_{i,Rie}$ appearing in Eq. (3) by saving a little CPU time, an equivalent formulation being easy to find for implementing the term $\langle \boldsymbol{\nabla} P \rangle_i + \boldsymbol{\Theta}^{\boldsymbol{u}}_{i,Rie}$.

C. Particle shifting technique with APR

Using a PST is common in SPH to maintain regular particle distribution, and becomes crucial when dealing with APR.[13,52,95] When mixed interactions are considered, PST has to be modified.[59,85] In the present section, the PST velocity retained for multi-resolution is detailed. It is based on the pioneer work of Lind *et al.* about PSTs based on Fick's law of concentration,[43] adapted to the weakly compressible assumption by Oger *et al.*,[63] improved in Ref. 55 in terms of consistency and invariance, with the limitation derived in Ref. 53 dedicated to quasi-Lagrangian formulations. The obtained PST velocity $\boldsymbol{\delta u}_i$ was used in the RHOD-SPH framework in Ref. 54, and its generic formulation is recalled in Sec. IV C 1. For more accurate results in multi-resolution, the gradient of concentration $\boldsymbol{\nabla} C_i$ is slightly modified with respect to Ref. 54, and details are provided in Sec. IV C 2.

1. PST velocity

As all PSTs are based on Fick's law, the first step consists of computing a non-dimensional vector $\boldsymbol{J}_i$ pointing toward zones of low concentration of particles, and, as in Ref. 55, it is expressed as

$$\boldsymbol{J}_i = -R_i \boldsymbol{\nabla} C_i, \tag{25}$$

$\boldsymbol{\nabla} C_i$ being the gradient of concentration, detailed in Sec. IV C 2. To ensure the kinematic free-surface condition, $\boldsymbol{J}_i$ has to be projected in the tangential direction. Different treatments have been proposed for this purpose in the literature.[32,55,79,80,91] In the present work, the treatment proposed in Ref. 55 is retained and consists of a progressive projection in the free-surface region. The projected vector reads:

$$\boldsymbol{J}^{\perp}_i = \boldsymbol{J}_i - \sigma_i (\boldsymbol{J}_i \cdot \tilde{\boldsymbol{n}}_i) \tilde{\boldsymbol{n}}_i, \tag{26}$$

with $\tilde{\boldsymbol{n}}_i$ the normal vector in the free-surface region and σ_i the projection function, both defined in Ref. 55. For inner fluid particles $\tilde{\boldsymbol{n}}_i = \boldsymbol{0}$. Finally, the PST velocity $\boldsymbol{\delta u}_i$ is computed as follows:

$$\boldsymbol{\delta u}_i = \boldsymbol{J}^{\perp}_i \min\left(a_i\, U^{char}_i\,; \quad b_i \frac{R_i}{\Delta x_i} \frac{U^{char}_i}{||\boldsymbol{J}^{\perp}_i||}\,; \quad \frac{\epsilon}{2\Delta t |\boldsymbol{J}^{\perp}_i \cdot \boldsymbol{\nabla}\Gamma_i|} \right); \qquad \boldsymbol{\nabla}\Gamma_i = \sum_j \boldsymbol{\nabla}_i W_{ij} V_j, \tag{27}$$

with (i) $U^{char}_i = \max_j\left(|(\boldsymbol{u}_j - \boldsymbol{u}_i) \cdot \frac{(\boldsymbol{x}_j - \boldsymbol{x}_i)}{||\boldsymbol{x}_j - \boldsymbol{x}_i||}| \right)$ the characteristic PST velocity, (ii) $a_i = 0.5$ the PST coefficient, (iii) $b_i = 0.05$ a protection against strong values of $\boldsymbol{J}^{\perp}_i$, and (iv) ϵ the maximum variation of density due to the shifting enabled during one time step Δt. The derivation of the latter term has been performed in Ref. 53 and in the present work the limitation is set to $\epsilon = 5 \times 10^{-4}$.

2. Gradient of concentration ∇C_i in APR

While $\boldsymbol{\nabla}\Gamma_i$ was used as a basis vector for the packing algorithm,[16] in the PST context a more "local" gradient of concentration is generally preferred. In Ref. 43, Lind *et al.* proposed to use

$$\boldsymbol{\nabla} C^{L.\,et\ al.}_i = \sum_j \left[1 + 0.2 \left(\frac{W_{ij}}{W(dx)} \right)^4 \right] \boldsymbol{\nabla}_i W_{ij} V_j; \quad dx = \Delta x, \tag{28}$$

with dx the targeted inter-particle size, i.e., $dx = \Delta x$ in single resolution. Therefore, when two particles i and j are closer than the characteristic distance Δx, their contribution in the computation of $\boldsymbol{\nabla} C^{L.et\ al.}_i$ is increased with respect to $\boldsymbol{\nabla}\Gamma_i$, as sketched in Fig. 3.

In APR with mixed interactions, Eq. (28) has to be modified as in Ref. 59. In the present work, the generalization of Fickian-based PST is performed by modifying the targeted inter-particle size as $dx_{ij} = \frac{\Delta x_i + \Delta x_j}{2}$. Consequently, the gradient of concentration is adapted to become the basis vector of Eq. (25) as

$$\boldsymbol{\nabla} C_i = \sum_j \left[1 + 0.2 \left(\frac{W_{ij}}{W(dx_{ij})} \right)^4 \right] \boldsymbol{\nabla}_i W_{ij} V_j; \quad dx_{ij} = \frac{\Delta x_i + \Delta x_j}{2}. \tag{29}$$

It is worth mentioning that Eqs. (29) and (28) are equivalent in the single-resolution context.

D. APR approach adopted in the present work

After recalling the RHOD-SPH scheme and having developed the generalization of Riemann terms and PST therein, the adopted APR technique can now be presented. As stressed in Sec. II, the adoption of an accurate pressure gradient within the RHOD-SPH

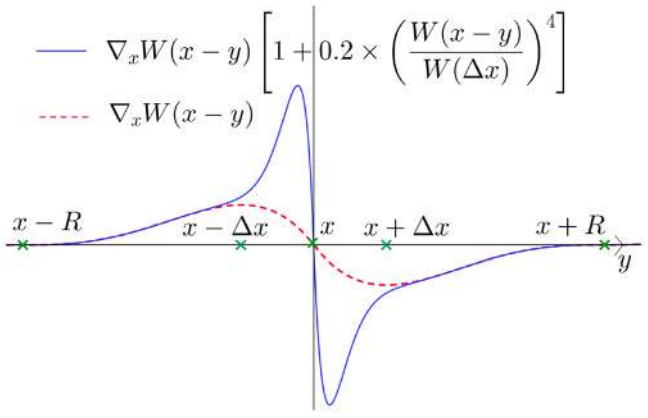

FIG. 3. Effect of the non-linear term of Eq. (28) in function of y.

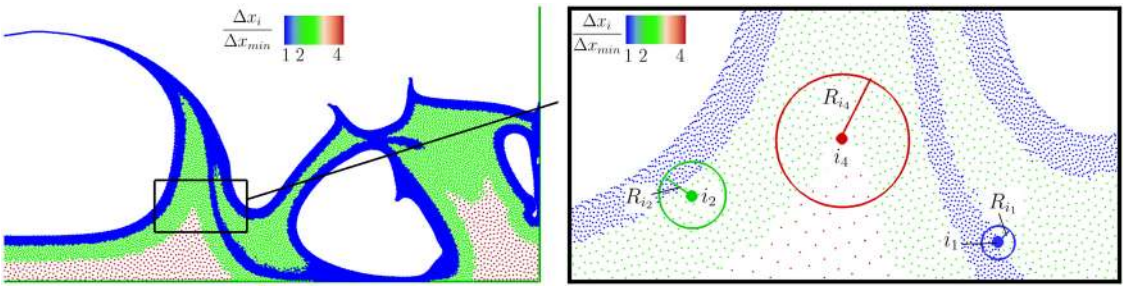

FIG. 4. Illustration of the present APR approach on a dam-break test case. Particles of different size Δx_i are represented with different colors. Δx_{min} stands for the minimum size in the simulation. A close-up is provided in the right plot where three particles i_1, i_2, and i_4 of different sizes are identified, with their kernel support and radius.

scheme enables the usage of Approach n.3 and extends it to free-surface flows thanks to the conservative form of the pressure gradient operator (6) in the free-surface region. This approach allows for large variations in particle size without requiring buffer regions or variations of the $h/\Delta x$ ratio. Each particle i has its own characteristic size Δx_i and kernel support radius R_i, with a fixed ratio $R_i/\Delta x_i$ for all particles; a ratio $R_i/\Delta x_i = 4$ is used all along the present work. Other values $R_i/\Delta x_i$ may also be employed. The influence of this parameter on the present APR scheme is discussed in the Appendix. As shown in Fig. 4, particles of significantly different size are mixed and interact with each other without the need of any predefined geometrical refinement box or buffer region. Furthermore, the robustness of the present approach enables the adoption of different refinement criteria, possibly based on specific regions of the flow (e.g., the proximity to a body or to the free surface) as well as on physical fields, as described in Sec. V and showcased in Sec. VI.

V. REFINEMENT PROCEDURE AND CRITERIA

To enlarge the range of applications achievable with the present multi-resolution technique, a refinement procedure is employed, divided into two steps. The first step consists of determining particles that require a refinement. This task is performed by considering some criteria, and a particle that fulfills these criteria is marked as "refinement required." The criteria are determined at the end of the current time step $t + \Delta t$ (precisely during the last stage of the time integration scheme). In the second step, the particles marked as "refinement required" enter a refinement procedure before starting the following time step. Criteria and refinement procedures are detailed in Secs. V A and V B.

A. Refinement procedure

As highlighted in Sec. II, different refinement procedures have been proposed in the SPH literature, both regarding the refinement pattern and the assignment of the physical quantities to the newly generated particles. In the present work, a particle i of size Δx_i marked as "refinement required" is split into four fine particles (called child particles) and noted i_{c1}, i_{c2}, i_{c3}, and i_{c4} as represented in Fig. 5. As in Ref. 13, the refinement pattern is a square of length $\Delta x_i/2$, the characteristic distances of the child particles (size, radius, smoothing length) being half the ones of the particle i. Other refinement patterns are possible and briefly discussed in the Appendix. The refinement pattern is oriented to maximize the minimum inter-particle distance once the refinement is completed, as sketched in Fig. 5.

Regarding the assignment of the physical quantities to the child particles, different strategies have been studied in the literature, as stressed in Sec. II. After some tests, we remark that, conversely to Ref. 30 and in agreement with Ref. 22, better results are obtained with a strategy ensuring conservation of mass, momenta, and kinetic energy. To ensure both linear momentum and kinetic energy conservation, the velocity of the child particles is the original velocity

$$\boldsymbol{u}_{i_{c1}} = \boldsymbol{u}_{i_{c2}} = \boldsymbol{u}_{i_{c3}} = \boldsymbol{u}_{i_{c4}} = \boldsymbol{u}_i.$$

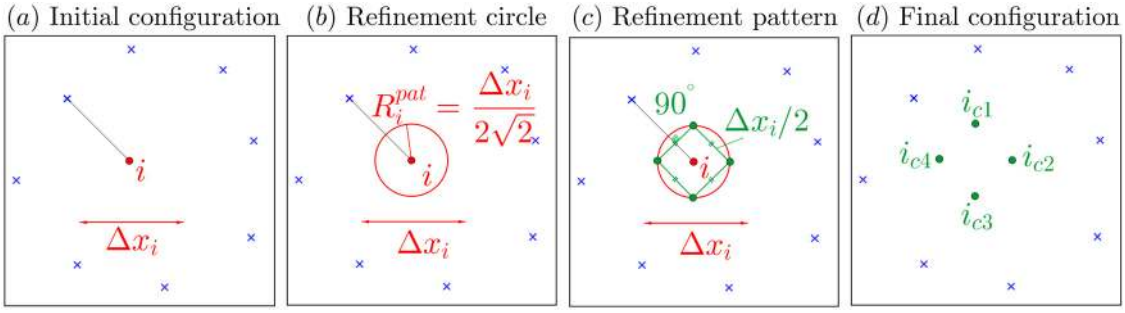

FIG. 5. Sketch of the refinement position pattern for a particle i of size Δx_i. (a) Initial configuration: the black line indicates the direction to the closest neighbor particle; (b) particle i is split into four particles of size $\Delta x_i/2$ located on a circle of radius $R_i^{pat} = \frac{1}{\sqrt{2}}\frac{\Delta x_i}{2}$. (c) The refinement pattern is a square with side length $\Delta x_i/2$, oriented in alignment with the black line in order to maximize particle spacing upon completion of the refinement. (d) Final configuration: child particles i_{c1} to i_{c4} are created and original particle i is deleted.

To ensure both mass and angular momentum conservation, the mass of particle i is equally distributed on the child particles

$$m_{i_{c1}} = m_{i_{c2}} = m_{i_{c3}} = m_{i_{c4}} = \frac{m_i}{4}.$$

Following Ref. 30, the pressure field is linearly projected, and the volumes are chosen to ensure equal distribution of mass, that is as

$$P_{i_{ck}} = P_i + \langle \nabla P \rangle_i^{\mathcal{L}} \cdot (\boldsymbol{x}_{i_{ck}} - \boldsymbol{x}_i); \quad \rho_{i_{ck}} = P_{i_{ck}}/c_0^2 + \rho_0;$$
$$V_{i_{ck}} = \frac{1}{\rho_{i_{ck}}} \frac{V_i \rho_i}{4}; \quad k = 1, \ldots, 4,$$

with $\langle \nabla P \rangle_i^{\mathcal{L}}$ computed following Eq. (14) with $\phi_i = P_i$. Note that the accuracy of the above projection is of the same order of accuracy as the pressure gradient approximation in Eq. (6).

B. Refinement criteria

In the present paper a particle i is marked as "refinement required" if one of the following criteria is fulfilled:

(1) i interacts with a "grandchild" particle, i.e., if $\exists j \in \mathcal{D}(i) : \Delta x_j = \Delta x_i/4$, where $\mathcal{D}(i)$ is the set of particles located inside the kernel support of particle i.
(2) i is isolated in a field of smaller particles, i.e., if $\sum_{j \in \mathcal{D}(i): \Delta x_j \geq \Delta x_i} \Gamma_{ij} < 2\,\Gamma_{ii}$.
(3) i belongs to the free-surface region, i.e., i interacts with a free-surface particle.
(4) i is close to a solid boundary, i.e., the kernel support of i intersects a solid panel.
(5) a physical quantity associated with i has, a value higher than a threshold value, i.e., if $\phi_i > \phi_{thr}$.

Criteria 1 and 2 are always activated, whereas criteria 3–5 depend on the targeted zone of interest and, therefore, on the targeted application. Criterion 1 stands for a stability criterion and is employed to prevent kernel issues of "grandchild" particles. Indeed, since a "gather"-type of interaction is retained in this work along with a ratio $\frac{R_i}{\Delta x_i} = 4$, the presence of a particle with size $4\Delta x_i$ in the kernel support would be an excessive coarseness in the summation integral and could result in an artificial void. Note that using such a criterion is a common practice in other numerical methods, like in finite volume method to avoid too large a size ratio between two adjacent cells.[90]

Criterion 2 is employed since there is no gain in keeping a particle surrounded by finer particles. Such a particle is then refined in order to retrieve a particle field of the same size, and the criterion is based on a Shepard approximation where Γ_{ij} is defined in Eq. (7). Note that in the present work, a minimum particle size Δx_{min} is imposed in the simulation, which is fixed prior to the simulation. Therefore, Δx_{min} cannot be exceeded. To this end, a necessary condition for i to be refined is that it is sufficiently coarse to handle another refinement, i.e., if $\Delta x_i/2 > \Delta x_{min}$.

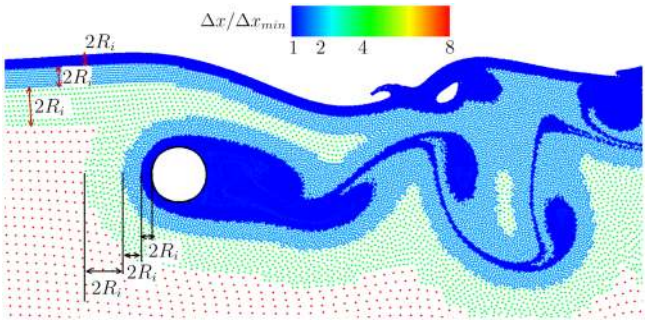

FIG. 6. Example of spatial resolutions obtained for a flow past an immersed cylinder when criteria 1–3 are activated. Criterion 4 is activated around the cylinder and disabled at the bottom part of the tank. Criterion 5 is not activated.

Criteria 3 and 4 can be activated depending on the zones of interest of the targeted application and, if several bodies are involved, criterion 4 can be activated only on selected bodies. It induces a thin zone of size $2R$ in which particles are all of same size $\Delta x = \Delta x_{min}$ and, thanks to the criterion 1, this is repeated for the successive refinement levels, as sketched in Fig. 6. Note that the initial particle setup is chosen to naturally ensure the criteria in order to avoid a refinement cascade at the beginning of the simulation.

The aim of APR is to retrieve the same results as those obtained with single-resolution, but at a lower CPU cost. For some applications criteria 3 and 4 are not sufficient, and criterion 5 is activated in such cases. In the present work a simple criterion is used: it is based on the pressure value, and a particle i is refined when a threshold pressure is exceeded. This threshold pressure depends on the considered application. A systematic use of this type of criteria deserves dedicated studies on several test cases in order to be generalized, which is left to future works. Nonetheless, the present study shows that the proposed formulation can also be effectively integrated with criteria based on field-dependent quantities.

VI. NUMERICAL DISCUSSION

This section is dedicated to the discussion of the numerical results. Six two-dimensional benchmarks are selected. The main purposes and refinement strategies are summarized in Table II and

TABLE II. Summary of active refinement criteria (see Sec. V B) and purposes of all numerical experiments.

Label	Test case	Active refinement criteria	Purpose
A	Hydrostatic	No dynamic refinement	Stability of the APR scheme
B	Rotating square	Criterion 3	Stability and accuracy of the free-surface refinement
C	Water entry	Criterion 4	Accuracy of the refinement near solid boundaries
D	Dam-break	Criterion 3	Robustness in presence of fragmentation and breaking
E	Flow past cylinder	Criteria 4 and 5	Effectiveness of the different refinement criteria
F	Flow past immersed cylinder	All criteria active	Robustness and accuracy of the overall scheme

TABLE III. Summary of physical and numerical constants in the simulations.

Test-case label	c_0	$\frac{L}{\Delta x_{min}}$	N. of ref. levels	Viscous/inviscid
A	$10\sqrt{gH}$	200	2	Inviscid
B	$10\,L\,\sigma_0$	800	3	$Re = 2000$
C	80 m/s	1000	7	Inviscid
D	$10\sqrt{gH}$	200	4	Inviscid
E	$10\,U_0$	75	4	$Re = 200$
F	$10\sqrt{g(h+H)}$	50	4	$Re = 180$

physical and numerical parameters in Table III. The results obtained are compared to both reference results and results obtained in single resolution.

As a first test, a hydrostatic case is considered. It acts as a demonstrative case to show the capability of Approach n.3 to deal with large Δx variations with a "gather"-type of interpolation and without the need for adapting the smoothing length h.

The second test case is the classic rotating square patch.[38] It represents a suitable and challenging case for studying the behavior of the proposed scheme when free-surface particles are continuously generated in the free-surface region subjected to large deformations. To the best knowledge of the authors, it is the first time that this case has been studied in the APR context.

The third test case consists in a water entry of a V-shaped body. Due to the large dimension of the tank, the refinement is essential in this test case, and it is therefore often used to validate APR techniques in the SPH community. It also represents a relevant test case to study the proposed scheme when particles are continuously generated close to solid boundaries.

The fourth benchmark is a dam-break case and represents one of the most popular cases in the SPH community. In the APR context, dam-break cases were studied with Approach n.1[97] and Approach n.2.[13] In the present work, the refinement is activated in the free-surface region, and this case is considered here to address the robustness of the proposed scheme in the presence of multiple free-surface reconnections.

Finally, flows past cylinders are considered. Flows past obstacles are classic cases in the APR context and have been analyzed using all three approaches.[30,59,78] In Sec. VI E, we start studying a classical flow past a cylinder in an unbounded domain at $Re = 200$. This benchmark is used to test different refinement strategies in a well-established framework. The outcomes of this test case are then used for the final validation case, which is one of the flows introduced in Ref. 9. In that problem the cylinder is placed below the free surface with a Froude number $Fr = 1$, generating vortical structures by both the cylinder and free-surface reconnections. For that test case, all the refinement criteria are activated.

A. Hydrostatic test case

In this case a fluid column of height H, width $L = 0.5H$, and nominal density ρ_0 is placed inside a tank of the same width and of height $2H$, as depicted in the left plot of Fig. 7. Two spatial resolutions are used depending on the relative position to a curve of equation $y = 0.25H\sin(\frac{2\pi x}{0.25H}) + 0.5H$, with the origin $[x = 0\,;\, y = 0]$ located at the bottom-left corner of the tank. Above that curve the particle size Δx is set to $\frac{H}{\Delta x} = 200$ whereas on the bottom part $\frac{H}{\Delta x} = 100$. The packing algorithm presented in Ref. 16 is applied independently within each subdomain to properly initialize the particle distribution. A zoom around a multi-resolution zone is provided in the right plot of Fig. 7 to highlight the effect of this procedure.

The initial velocity is set to $\boldsymbol{u} = \boldsymbol{0}$ and the initial pressure is the analytical solution of the compressible hydrostatic pressure $P^{an} = \rho_0 c_0^2[e^{(\boldsymbol{x}-\boldsymbol{x}_{FS})\cdot\boldsymbol{g}/c_0^2} - 1]$ with $\boldsymbol{g}$ the gravity vector and $\boldsymbol{x}_{FS}$ a point located on the free surface. The speed of sound is set to $c_0 = 10\sqrt{gH}$ following the weakly compressible assumption (2) The reference scales are the length H, the time $\sqrt{H/g}$, the pressure $\rho_0 gH$, and the energy $V\rho_0 gH$ with V the volume of fluid. Criteria 4 and 5 are not considered.

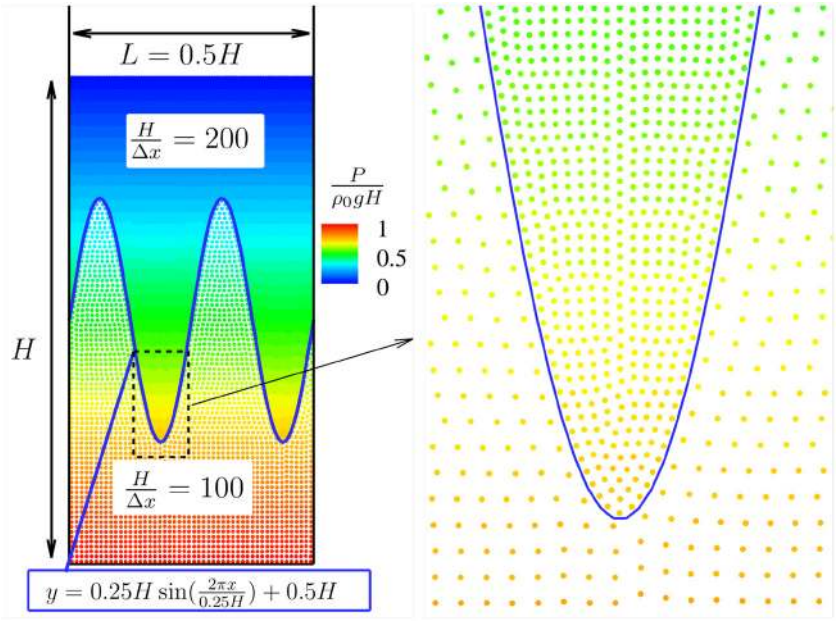

FIG. 7. Hydrostatic test case. Initial setup of the case. A zoom is provided in the right plot to highlight the effect of the packing algorithm.

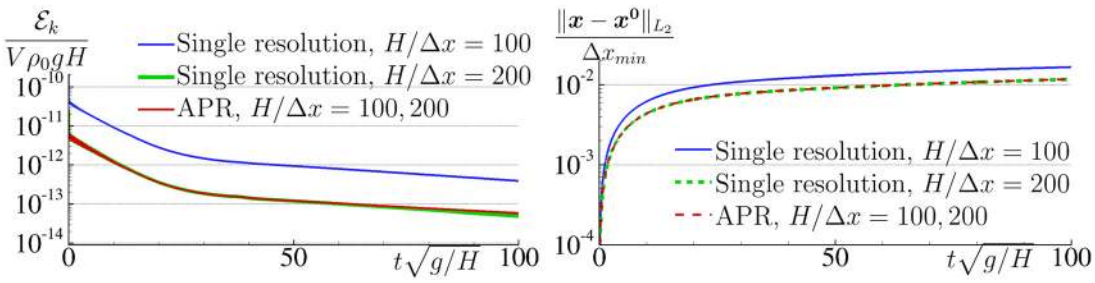

FIG. 8. Hydrostatic test case. Left: temporal evolution of the kinetic energy $\mathcal{E}_k$. Right: temporal evolution of the particle displacement in L_2 norm where $||\boldsymbol{x}-\boldsymbol{x}^0||_{L_2} = \sqrt{\frac{\sum_i ||\boldsymbol{x}_i-\boldsymbol{x}_i^0||^2 V_i}{V}}$. The results obtained with the present APR are compared to those obtained in single resolutions $H/\Delta x = 100$ and $H/\Delta x = 200$.

Thus, the refinement procedure is never activated for this test case. As stressed in Sec. II, these large Δx variations using Approach n.1 would require smooth variations of h, whereas Approach n.2 seems hardly applicable due to the geometrical shapes of the refined zones. Consequently, this benchmark is a demonstrative case to show the benefits of Approach n.3, i.e., using the accurate pressure gradient approximation defined in Eq. (6) with mixed interactions. To validate quantitatively the present formulation, results obtained with single resolution are also given.

In Fig. 8, the temporal evolution of the kinetic energy and particle displacement obtained with the present APR scheme are reported and compared to single-resolution cases. The kinetic energy $\mathcal{E}_k$ obtained with the APR scheme remains below 10^{-11} of the reference energy $V\rho_0 gH$ during all the simulation. A permanent decay is observed, reaching $\frac{\mathcal{E}_k}{V\rho_0 gH} < 10^{-13}$ at $t\sqrt{g/H} = 100$. This result reflects the small variations in the particle displacement occurring during the simulation. Indeed, as visible in the right plot, the particle displacement at $t\sqrt{g/H} = 100$ is such that $\sqrt{\frac{\sum_i ||\boldsymbol{x}_i-\boldsymbol{x}_i^0||^2 V_i}{V}} \simeq 10^{-2}\,\Delta x_{min}$, being $\boldsymbol{x}_i^0$ the position of particle i at $t = 0$. In other words, at the end of the simulation an average displacement of $10^{-2}\,\Delta x_{min}$ is noted with respect to the initial position. The results obtained in APR are very similar to those obtained in single-resolution $H/\Delta x = 200$.

The temporal evolution of the pressure error with respect to the analytical solution is reported in the left plot of Fig. 9, both in norms L_1 and L_∞. The results obtained in APR are superimposed on the single-resolution result $H/\Delta x = 200$, with an L_1-error smaller than 0.1% of the reference pressure during all the simulation. The gap between the L_∞ and L_1 norms is due to the free-surface particles where the error is concentrated and is related to the conservative pressure gradient approximation used in that region. As shown in the right plot, the pressure field obtained at $t\sqrt{g/H} = 100$ using the APR scheme remains smooth, including across the interface between the two resolution levels. Finally, the number of particles and the CPU time required for these simulations are reported in Table IV. A reduction of the computational costs of about 25% is achieved for the same level of accuracy of the resolution $H/\Delta x = 200$.

B. Rotating square patch at *Re*=2000

In the present section, a classical benchmark is studied where large free-surface deformations are involved.[14,32,38,54,79] It consists of an initial square fluid domain of length L, in which the velocity field is

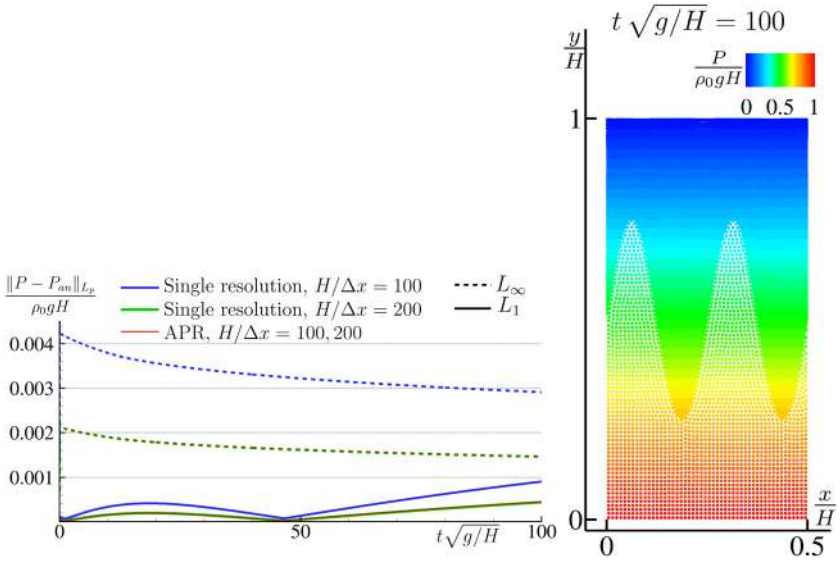

FIG. 9. Hydrostatic test case. Left: temporal evolution of the pressure error with respect to the analytical solution obtained with the present APR, compared to those obtained in single resolutions $H/\Delta x = 100$ and $H/\Delta x = 200$; in dashed lines L_∞ pressure error; in solid lines L_1 pressure error defined as $\frac{\sum_i |P_i - P_i^{an}| V_i}{V}$. Right: pressure field obtained with the present APR scheme at $t\sqrt{g/H} = 100$.

TABLE IV. Hydrostatic test case. Comparison between APR and single resolutions $H/\Delta x = 100$ and $H/\Delta x = 200$ in terms of number of particles and CPU time at $t\sqrt{g/H} = 100$. A single core on a workstation machine equipped with 48 cores Intel(R) Xeon(R) Gold 5220R CPU at 2.20 GHz has been used in the three cases.

	$H/\Delta x = 100$	$H/\Delta x = 200$	$H/\Delta x = 100, 200$
Number of particles	5000	20 000	12 460
CPU time	3 h 38 min	24 h 50 min	18 h 0 min

initialized with a uniform angular velocity $-\sigma_0$; the center of rotation is the center of the square. The initial velocity and pressure are

$$\begin{cases} u_x = \sigma_0 y, \\ u_y = -\sigma_0 x, \\ p = \rho_0 \sum_{m=1}^{\infty}\sum_{n=1}^{\infty} \dfrac{-32\sigma_0^2}{mn\pi^2\left[(n\pi/L)^2 + (m\pi/L)^2\right]} \sin(m\pi x/L)\sin(n\pi y/L), \end{cases} \tag{30}$$

and the reference variables are the length L, the time $1/\sigma_0$, the velocity $L\sigma_0$, the pressure $\rho_0 L^2\sigma_0^2$, the vorticity $2\sigma_0$ and the initial kinetic energy $\mathcal{E}_k^0$. The speed of sound is chosen as $c_0 = 10\,L\sigma_0$. The pressure is negative in all the fluid domains with an adverse pressure gradient at the free surface. Therefore, Rayleigh–Taylor instability is expected to appear. To prevent these instabilities, it is necessary to add a sort of viscosity to the fluid, either artificial or physical. As in Ref. 54, we preferred the latter choice to avoid a dependence of the viscosity on the spatial resolution (as for the artificial viscosity). The corresponding Reynolds number is chosen as in Ref. 54 as $Re = 2000$ with $Re = \rho_0 L^2\sigma_0/\mu$. The particles are initialized as represented in Fig. 10, that is, with a spatial resolution $L/\Delta x = 200$ inside a disk of radius $R_{200}/L = 0.44$, $L/\Delta x = 400$ inside a circular ring of internal and external radii $R_{200}/L = 0.44$ and $R_{400}/L = 0.48$, respectively, and $L/\Delta x = 800$ elsewhere. The particle packing algorithm[16] is used for a better initial particle distribution.

Refinement criteria 1–3 are used. This test case represents a suitable and challenging benchmark for validating the refinement procedure in the free-surface region, as the free surface is subjected to large deformations and, therefore, new particles are continuously generated (see right plots of Fig. 11). The vorticity field at different instants is plotted in the left part of Fig. 11 and displays a continuous behavior, even in zones of large Δx variations. The free-surface shape is compared to the one obtained in single-resolution $L/\Delta x = 800$, the latter having already been validated against reference results in Ref. 54. A good agreement is found all along the simulation. Only small differences are observed from t/σ_0 in the patch center, which are acceptable in light of the fluid flow evolution complexity.

This good agreement is confirmed in Fig. 12, where the temporal evolution of the kinetic energy is compared to the one obtained with the single resolutions $L/\Delta x = 200$, $L/\Delta x = 400$, and $L/\Delta x = 800$. Since the APR simulation is composed of particles of these different sizes, the expected behavior of an accurate APR scheme is an energy dissipation located somewhere between the one obtained with the single resolutions $L/\Delta x = 200$ and $L/\Delta x = 800$. In fact, the kinetic energy is close to the one obtained with $L/\Delta x = 400$, with a relative error of 0.36% with respect to $L/\Delta x = 800$ at $t/\sigma_0 = 10$. Since momenta are not formally conserved with the present scheme, we monitored the angular momentum conservation. The L_1 norms of the error with respect to the analytical solution (initial angular momentum) are 0.037% for the highest single-resolution ($L/\Delta x = 800$) and 0.098% for the APR solution. This difference is visible in Fig. 13, where a discrepancy between single-resolution and APR free-surfaces is observed in the central region of the flow. Nevertheless, the overall evolution of the fluid flow shows no significant alteration. It is worth remarking that this test case is very challenging for an APR technique, and significant benefits in terms of CPU cost vs accuracy are not expected. The scope of the present test case is more on testing if the APR can manage such complex free-surface conditions.

C. Water entry of a 2D V-shaped body

Here, we consider the case of a V-shaped section impacting a free surface initially at rest, based on the experimental study conducted by Zhao *et al.*[100] This scenario serves as an ideal application for APR schemes, as the area of interest is concentrated around the impact zone, allowing for a significant reduction in spatial resolution elsewhere.[62,71] In this experimental campaign, a free-falling V-shaped body with a dead-rise angle 30°, assumed as symmetric and perfectly rigid, is released above the quiescent water. The recorded velocity before entering the liquid surface is $u_0(z) = -6.15\text{ms}^{-1}$ (see also the

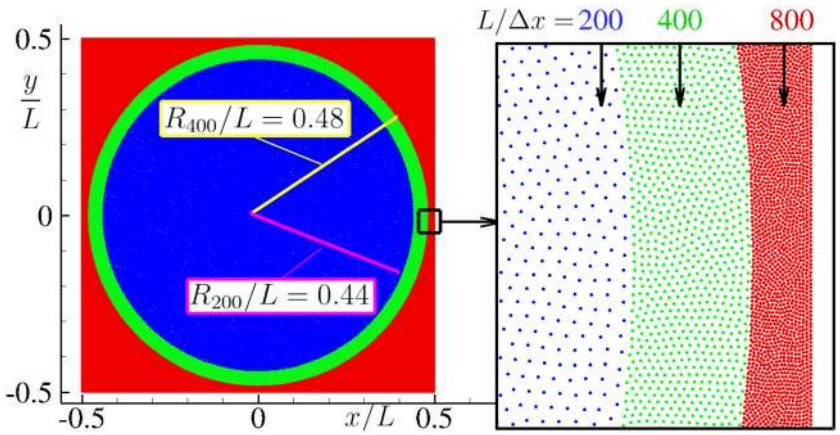

FIG. 10. Rotating square patch at $Re = 2000$. Initial particle distribution: $L/\Delta x = 200$ inside a disk of radius $R_{200}/L = 0.44$, $L/\Delta x = 400$ inside a circular ring of internal and external radii $R_{200}/L = 0.44$ and $R_{400}/L = 0.48$, respectively, and $L/\Delta x = 800$ elsewhere.

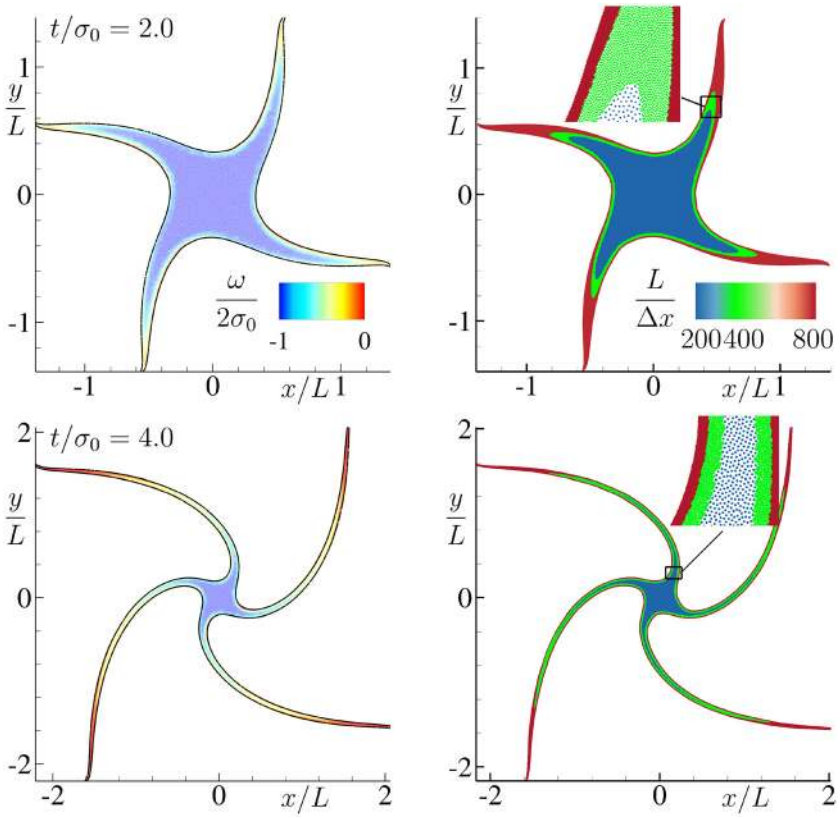

FIG. 11. Rotating square patch at $Re = 2000$. Left: vorticity field obtained at different instants $t/\sigma_0 = 2$, 4 (from top to bottom). Right: spatial resolution Δx_i at the same instants. In the left plot, the black line stands for the free surface obtained with a single-resolution SPH $L/\Delta x = 800$.

left plot of Fig. 14). The body is equipped with an accelerometer, force transducers, and five pressure sensors placed along a surface section of breadth 20 cm. The experimental setup is completed with two dummy sections (for an overall breadth of 1 m) and a drop rig for a total free-falling mass of 255.5 kg. All degrees of freedom are inhibited except the vertical motion. Following the work by Ref. 62, here we choose to consider a freely falling body rather than a body with imposed vertical motion.

One of the main challenges in simulating this problem within a 2D numerical framework is the presence of significant 3D effects, resulting from the relatively short breadth b of the body compared to its length l ($l = 0.5$ m in the x-direction and $b = 1$ m in the y-direction). Note that this difficulty was already outlined in Ref. 100, in which the authors also compared their experimental results with numerical solutions obtained from a fully non-linear method based on potential theory.[70]

As sketched in Fig. 14, the initial particle distribution is performed with seven levels of particle refinement (from Δx_7 down to $\Delta x_{min} = \Delta x_1$) and, as in Refs. 62 and 71, the finest particles are of size $\Delta x_1 = 0.5$ mm. These particles are placed in a small rectangle of dimension [528 mm; 8 mm] and the particle size is progressively increased up to $\Delta x_7 = 32$ mm close to the tank border. Precisely, particles of size Δx_k are placed in nested rectangles of sizes $[528 + 16 \times \sum_{l=2}^{k} \Delta x_l; 8 + 8 \times \sum_{l=2}^{k} \Delta x_l]$ (unit measure is mm), that is, keeping eight particles between two rectangles in order to fulfill criterion 1. The resulting number of particles is 31 496 at the initial instant and grows to 42 839 at $t = 0.025$ s. Compared to Approach n.2 (see also Fig. 16), a significantly smaller number of particles is required. We take advantage of this to verify whether the chosen Δx_{min} is sufficiently small to accurately capture the fluid flow solution. To this end, two additional cases with more refined particles, $\Delta x_{min} = 0.25$ mm and $\Delta x_{min} = 0.125$ mm, were tested. No significant differences have been observed with respect to $\Delta x_{min} = 0.5$ mm (see left plot of Fig. 15), justifying the latter choice to complete the validation. Note that 13 min were required for the APR case with $\Delta x_{min} = 0.5$ mm on 8 processors, while for the single-resolution case with $\Delta x = 0.5$ mm, 20 h 54 min were needed on 48 processors. Both cases ran on the same machine equipped with 48 cores Intel(R) Xeon(R) Gold 5220R CPU at 2.20 GHz. As in Ref. 71 the sound speed is chosen as $c_0 = 80 \text{ms}^{-1}$.

The results obtained with the present APR are compared to both those obtained in single-resolution and reference results. The temporal evolution of the vertical forces F_Z exerted by the fluid on the body is represented in Fig. 15. Similar results are obtained between single and APR cases (see left plot). The comparison with reference results is plotted in the right plot, and a good agreement is found with the other APR approaches in SPH. The difference observed with the experimental results is due to the 3D effects as mentioned above. This good agreement is confirmed by the results in Fig. 16, where the pressure field is plotted at three different instants and compared to both the single-resolution and results from Ricci *et al.*[71] It is worth noting that the present APR approach allows recovering a pressure field as smooth as the single-resolution case, even in transition zones where the spatial

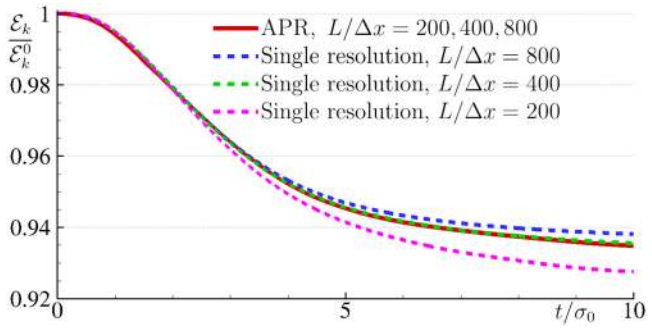

FIG. 12. Rotating square patch at $Re = 2000$. Temporal evolution of the kinetic energy $\mathcal{E}_k$ obtained in APR with $L/\Delta x = 200$, 400, and800 compared to the one obtained in single-resolution configurations with $L/\Delta x = 200$, $L/\Delta x = 400$, and $L/\Delta x = 800$. $\mathcal{E}_k^0$ is the kinetic energy at $t = 0$.

resolution changes significantly. Additionally, the pressure peak is not affected by the multi-resolution, showing the advantages of Approach n.3 with respect to Approach n.2 in terms of the number of particles saved.

The pressure profile along the body at different instants is represented in Fig. 17. For comparison purposes, the reference scales have been obtained using the recorded motion given in Ref. 100, whose numerical values are reported in Table V. At all three considered time instants, the APR and single-resolution results are practically overlapping, exhibiting a smooth pressure profile. Comparisons with reference results are fair for t_2 and t_3, whereas more pronounced differences are observed for t_1, particularly for the pressure peak location. This is expected since t_1 corresponds to an early stage of the impact, and therefore the pressure peak is more localized than instants t_2 and t_3. The bottom-right plot of Fig. 17 depicts the particle size distribution against the pressure field. In this case, for better visualization, the particles are represented as circles with sizes proportional to Δx_i. This highlights again the smoothness of the pressure field in comparison to the steep gradient of the particle size.

Finally, Table VI reports the errors between single-resolution and APR solutions in L_2 and L_∞ norms for the force F_z of Fig. 15 and the pressure profiles of Fig. 17. Each value is reported in percentage with respect to the same norm of the single-resolution result; that is, $L_P = \frac{||F^{APR} - F^{SR}||_P}{||F^{SR}||_P}$ where the apex ^{SR} refers to the single-resolution result. L_2 norms are all below 5% error, whereas L_∞ ones are around 10%. In more detail, the error norms of the force signal F_z are lower than the pressure ones and well below 5%. This is expected for an integrated quantity.

D. Inviscid dam-break

The fourth test case studied is a dam-break flow impacting a vertical wall. It represents one of the most popular cases in the SPH community. Several setups have been studied in the literature, both experimentally and numerically. In the present work, the experiments

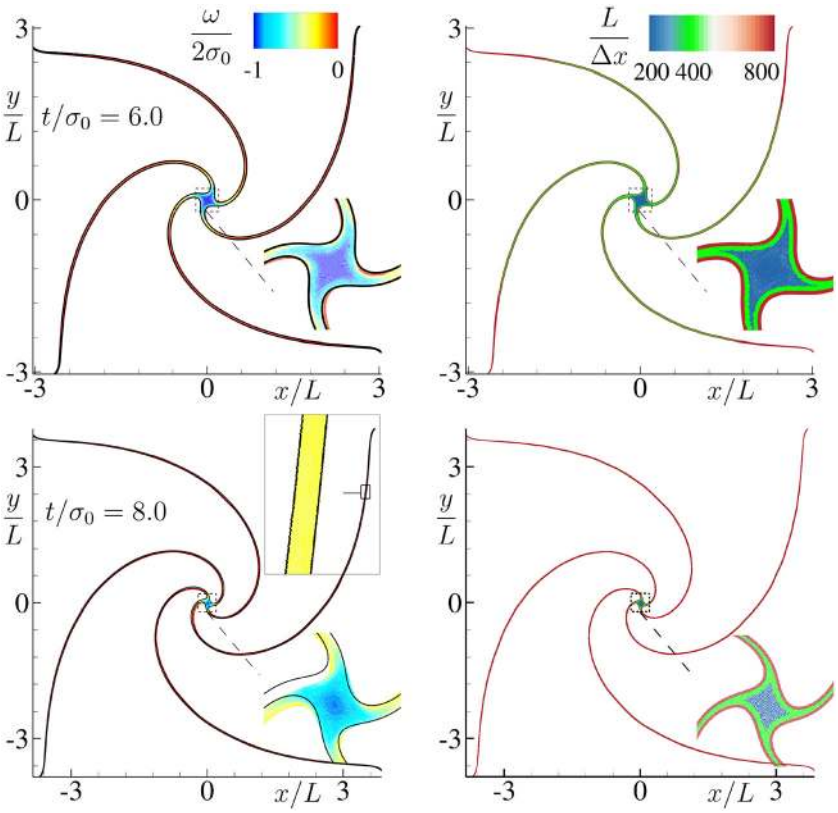

FIG. 13. Rotating square patch at $Re = 2000$. Left: vorticity field obtained at different instants $t/\sigma_0 = 6$, 8 (from top to bottom). Right: spatial resolution Δx_i at the same instants. In the left plot, the black line stands for the free surface obtained with a single-resolution SPH $L/\Delta x = 800$.

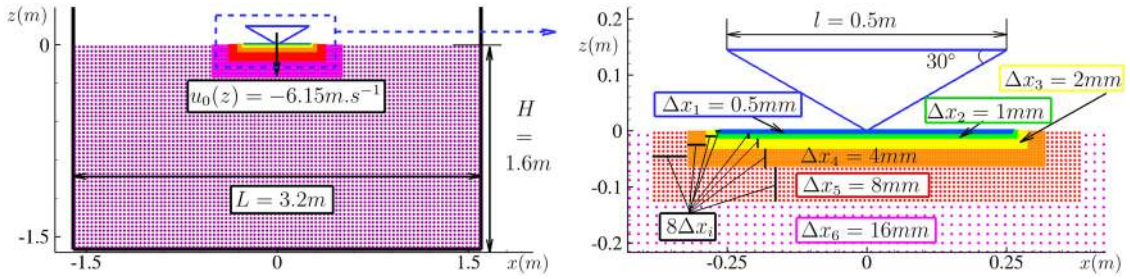

FIG. 14. Water entry of a 2D V-shaped body. Geometry and initial particle distribution. Left: global view of the particle size Δx. Right: zoom around the V-shaped body. Seven different particle sizes Δx are used, starting from $\Delta x_1 = 0.5$ mm close to the body up to $\Delta x_7 = 32$ mm close to the tank border, with a ratio $\Delta x_k/\Delta x_{k-1} = 2$ between two adjacent resolution levels. Each resolution level is arranged based on the refinement criteria outlined in Sec. VA, ensuring that each level has a minimum thickness of 8 Δx.

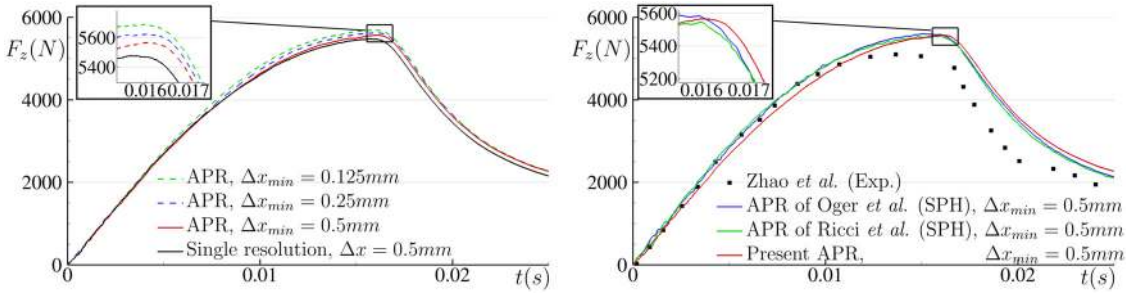

FIG. 15. Water entry of a 2D V-shaped body. Temporal evolution of the vertical forces exerted by the fluid on the body. Left: comparison of the present APR technique for three values of Δx_{min} with the single resolution using $\Delta x_{min} = 0.5$ mm. Right: comparison of the present approach with other reference solutions from the literature, all with $\Delta x_{min} = 0.5$ mm.

performed by Lobovský *et al.*[46] are retained, as represented in the left plot of Fig. 18. The reference scales are the length H, time $\sqrt{H/g}$, velocity $\sqrt{Hg}$, and pressure $\rho_0 gH$. After the first impact on the vertical wall, the fluid flow is characterized by free-surface fragmentation and multiple breaking processes. Within the APR context, dam-break cases were studied with Approach n.1[97] and Approach n.2.[13] In Ref. 13, the finest particles were concentrated in a rectangular zone close to the pressure patch on the opposite vertical wall. In Ref. 97, a dynamic splitting close to both the free-surface and solid boundaries was used, with a maximum Δx variations of 2.8 between the finest and coarsest particles. Therefore, it represents an accurate test case to check the robustness of Approach n.3 with high Δx variations. Refinement criteria 1–3 are used and the artificial speed of sound is chosen as $c_0 = 10\sqrt{Hg}$. A maximum spatial resolution of $H/\Delta x = 200$ is used and concentrated in the free-surface region. The initial particle configuration is chosen in line with the refinement in the free-surface region, as drawn in the right plot of Fig. 18. Note that in Ref. 26 it was studied with a constant spatial resolution $H/\Delta x = 200$. Due to the high Reynolds number involved in the experiments, the hypothesis of an inviscid fluid is used here. Parallelly, to avoid an overestimated numerical boundary layer due to the particle size used, a free-slip boundary condition is considered. As a consequence, there is no need for refining particles close to solid boundaries; that is, to activate criterion 4.

In Fig. 19, the pressure field is represented at different instants. The free-surface shape obtained with the single-resolution $H/\Delta x = 200$ is added for comparison purposes. Before the free-surface reconnection around $t\sqrt{g/H} \approx 6.15$, i.e., for a potential fluid flow evolution, APR and single-resolution results are similar, as visible in the top plots of the figure. Differences start to occur after the interface reconnection (bottom part of the figure), but even after the cavity closure, where the fluid flow evolution becomes chaotic, the principal trends observed in single-resolution are well captured in APR. Note that two-phase effects are missing during the multiple cavity closure events,[26] the results are, however, shown until $t\sqrt{g/H} = 10$ to highlight the robustness of the present formulation, even in the presence of free-surface fragmentation and reconnection. Remarkably, the pressure field is smoothed even in zones of large variations of Δx all along the simulation.

APR and single resolution with $H/\Delta x = 200$ are compared in terms of number of particles and CPU time at different instants in Table VII. At $t\sqrt{g/H} = 3$, both the number of particles and CPU time are more than 4 times lower in APR for similar results (see also the left plot of Fig. 20), thus representing a non-negligible advantage for studying the impact on the right vertical wall event. Please note that the CPU time is obtained on a workstation equipped with 48 cores Intel(R) Xeon(R) Gold 5220R CPU at 2.20 GHz. Furthermore, the APR scheme is implemented in a research code, which is not optimized to fully exploit the potential efficiency of the present approach. Since no coalescing procedure is used, the number of particles increases during the simulation, and the difference between APR and single resolution decreases. However, APR remains two times faster

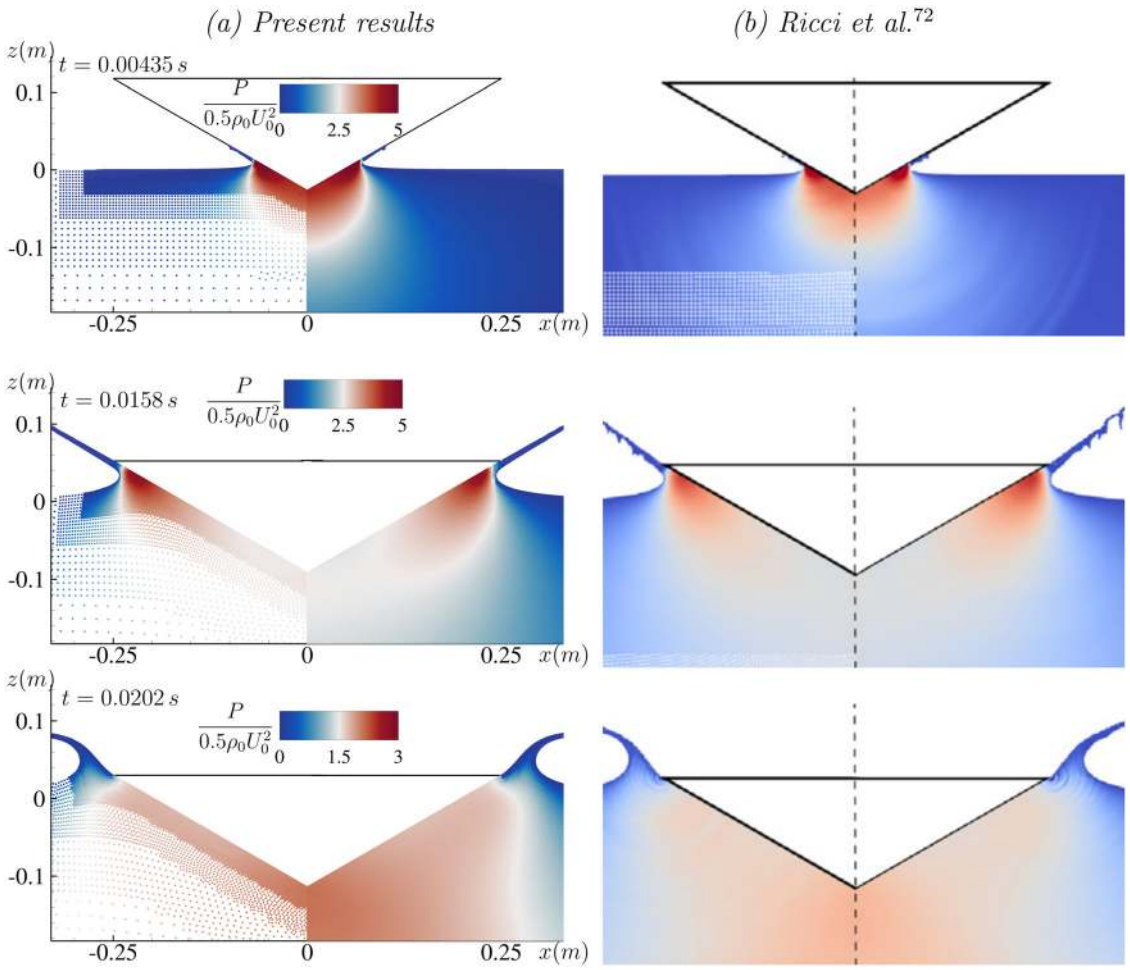

FIG. 16. Water entry of a 2D V-shaped body. Pressure profile obtained at $t = 0.00435$ s, $t = 0.0158$ s and $t = 0.0202$ s (from top to bottom). Left column: results obtained with the present formulation. Right column: results obtained by Ricci *et al.*[71] Contour levels are similar to those of Ref. 71 for qualitative comparison purposes. On each plot, the APR results are represented for $x < 0$; single-resolution results correspond to $x \geq 0$. Reproduced with permission from Ricci *et al.*, Comput. Methods Appl. Mech. Eng. **418**, 116500 (2024). Copyright 2024 Authors, licensed under a Creative Commons Attribution License.

from $t\sqrt{g/H} = 7$ to $t\sqrt{g/H} = 10$, for comparable results. Then, although this test case was mainly studied to address the robustness feature of the proposed APR scheme, the latter has proved to be efficient in any case.

APR results are compared quantitatively to both single-resolution and reference results in Fig. 20, where the temporal evolution of the pressure at probe P1 (located at $y = 0.01H$ on the right vertical wall) is plotted. APR and single resolution provide similar results, the main difference occurring after the interface reconnection at $t\sqrt{g/H} \approx 6.15$ where the fluid flow evolution becomes chaotic. The results are also similar to those of Hammani *et al.*[26] using δ-SPH and of De Courcy *et al.*[18] using incompressible SPH, both in terms of time needed for impacting the right vertical wall and global trends. High-frequency noise was appearing in Ref. 26 from $t\sqrt{g/H} \approx 5.2$, which is absent with the present formulation. This beneficial effect is due to the addition of the acoustic damper term[81] in the present model, thus recovering results very similar to the incompressible solution in Ref. 18. During the experimental campaign by Lobovský *et al.*,[46] a reproducibility investigation was carried out. Statistics were then performed, and the average and some percentile values were provided. In Fig. 20, the yellow zone corresponds to the area between the 2.5% and 97.5% percentile values. As observed, the pressure peak is well captured with the present model. Nevertheless, the impact on the right vertical wall occurs slightly before the experiments, and this aspect can be due to the initial gate opening (not simulated here) or to the friction between the water and the bottom wall. After the impact event, the global trend is retrieved with the present model, with a pressure overestimated from $t\sqrt{g/H} = 3$ to $t\sqrt{g/H} = 5$. Around $t\sqrt{g/H} = 5.85$, 3D effects are visible in the experiments with multiple air entrapments, which are obviously not captured with this single-phase 2D model. Then, 3D multiphase simulations should be conducted as in Ref. 56, for instance, which is left to future work.

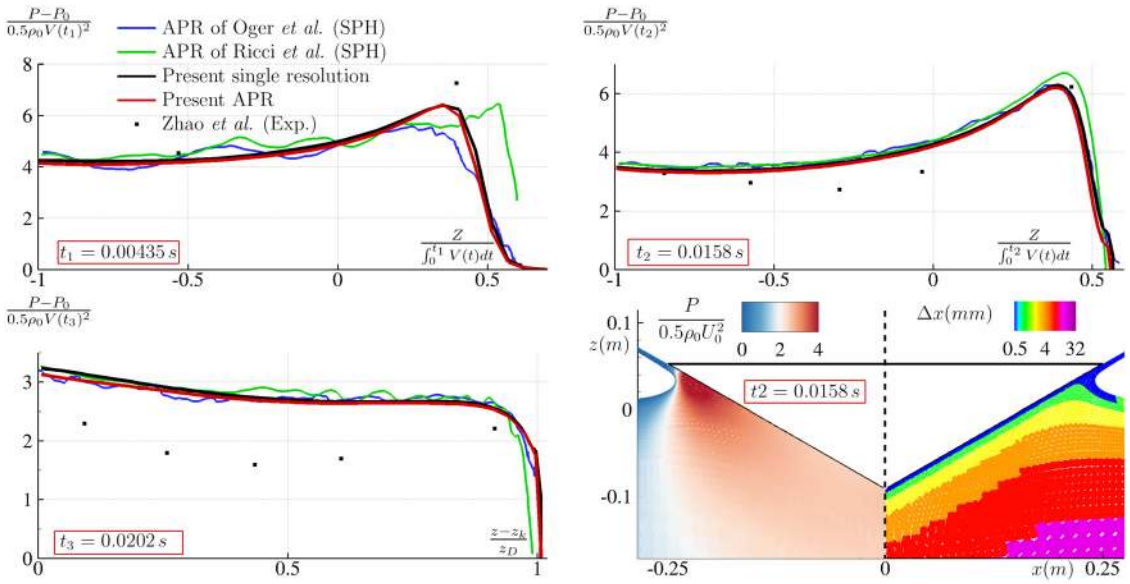

FIG. 17. Water entry of a 2D V-shaped body. Top-left, top-right, and bottom-left plots: pressure profile along the body at different instants compared to both single-resolution and reference results: $t = 0.00435$ (top left), $t = 0.0158$ (top right), and $t = 0.0202$ (bottom left); the legend is indicated only on the first plot for ease of readability. The reference scales used in these plots are reported in Table V. Bottom right: results obtained at $t = 0.0158$ (the size of the circles is based on their actual Δx_i); the pressure field is represented on the left side of the vertical dashed line at $x = 0$ whereas the spatial resolution is plotted on the right side.

TABLE V. Water entry of a 2D V-shaped body. Reference velocities and lengths used for the non-dimensionalization at times $t_1 = 0.004\,35$ s, $t_2 = 0.0158$ s, and $t_3 = 0.0202$ s. $V(t)$ is the velocity recorded in the experiments.[100] z_k and z_D stand for the vertical coordinate of the keel and draft of the body, respectively.

Time (in s)	$t_1 = 0.004\,35$	$t_2 = 0.0158$	$t_3 = 0.0202$
Velocity references for $\frac{1}{2}\rho_0 V(t_i)^2$ (in ms^{-1})	$V(t_1) \approx -6.1008$	$V(t_2) \approx -5.3094$	$V(t_3) \approx -5.0329$
Length references (in m)	$\int_0^{t_1} V(t)dt \approx -0.02668$	$\int_0^{t_2} V(t)dt \approx -0.09255$	$z_k \approx -0.1152$ $z_D = 0.25 \times \tan(30^\circ)$

TABLE VI. L_2 and L_∞ norms of the difference between single-resolution and APR solutions for the water entry simulation, in relation to the quantities presented in Figs. 15 and 17. Each value is reported in percentage with respect to the same norm of the single-resolution result, that is, $L_P = \frac{||F^{APR} - F^{SR}||_P}{||F^{SR}||_P}$ where the apex ^{SR} refers to the single-resolution result. Particle size equal to $\Delta x = 0.5$ mm is used for the single resolution and $\Delta x_{min} = 0.5$ mm for the APR simulation.

Quantity	F_z	$P(t_1)$	$P(t_2)$	$P(t_3)$
Error in L_2	2.4%	4.2%	4.0%	3.2%
Error in L_∞	3.5%	10.2%	11.4%	3.7%

E. Flow past a cylinder at *Re*=200

Before addressing the problem of the flow past a cylinder below the free surface, the proposed APR scheme is tested on a simpler and well-established benchmark, i.e., a flow past a cylinder in an infinite domain. The numerical domain is sketched in Fig. 21, where d is the cylinder diameter, U_0 is the free-stream velocity and $H = 40d$. This is a classical test in CFD where a large variety of Reynolds numbers have been studied.[40] In this work, $Re = U_0 d/\nu = 200$ is considered for which many reference results are available in the literature.

The speed of sound is $c_0 = 10U_0$. In order to anticipate the inception of the vortex shedding, an initial motion $y_C(t) = 0.1d\cos(2tU_0/d - \pi)$ is imposed on the y-coordinate of the cylinder center in the time frame $tU_0/d \in [0; 2\pi]$.

Different refinement strategies are tested:

(a) a simple refinement box of circular shape and diameter equal to $6d$ centered at the cylinder's midpoint;
(b) refinement only close to the solid body, i.e., criterion 4;
(c) both criteria 4 and 5.

Note that the strategy (a) is employed with a sufficiently large refinement box to be considered equivalent to a single-resolution case. Criterion 5 is based on the pressure field and is activated when

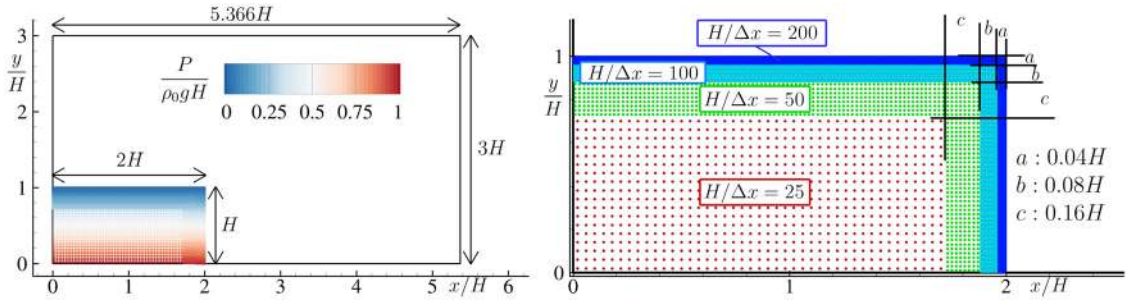

FIG. 18. Inviscid dam-break. Setup of the case (left plot) and initial particle distribution (right plot).

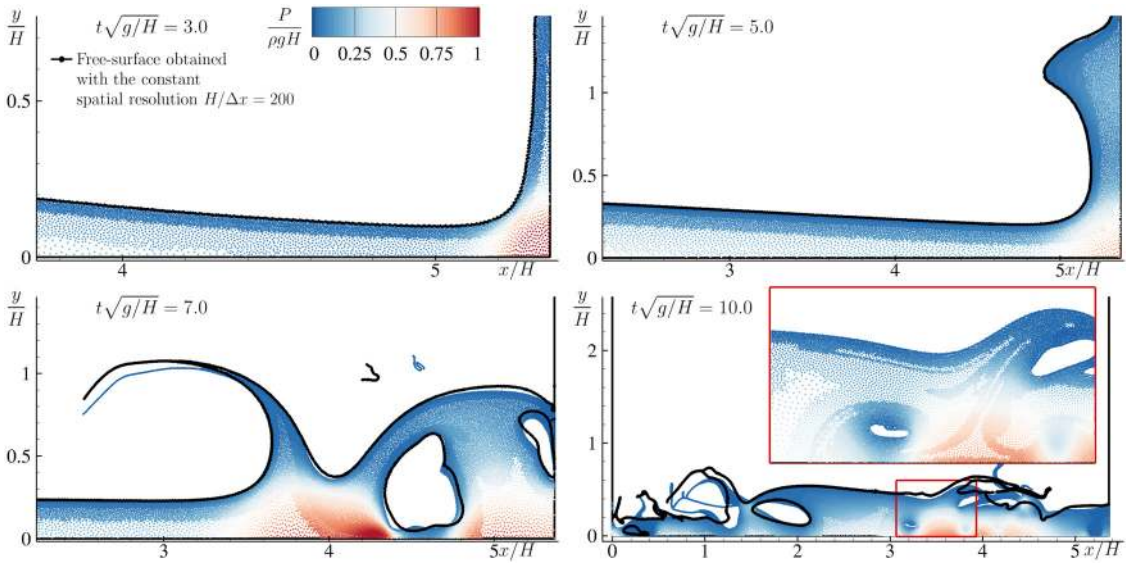

FIG. 19. Inviscid dam-break. Pressure field obtained at $t\sqrt{g/H} = 3$, $t\sqrt{g/H} = 5$, $t\sqrt{g/H} = 7$, and $t\sqrt{g/H} = 10$ (from top left to bottom right). On each plot, the black line corresponds to the free-surface shape obtained in single-resolution $H/\Delta x = 200$.

TABLE VII. Inviscid dam-break. Comparison between APR and single $H/\Delta x = 200$ resolutions in terms of number of particles and CPU time at different instants $t\sqrt{g/H} = 3, 5, 7, 10$. Eight processors on a workstation machine equipped with 48 cores Intel(R) Xeon(R) Gold 5220R CPU at 2.20 GHz have been used in both cases.

	$t\sqrt{g/H} = 3.0$	$t\sqrt{g/H} = 5.0$	$t\sqrt{g/H} = 7.0$	$t\sqrt{g/H} = 10.0$
Single resolution	80 000 (25 min)	80 000 (43 min)	80 000 (60 min)	80 000 (106 min)
APR	18 039 (6 min)	24 900 (12 min)	32 463 (20 min)	49 642 (38 min)

$$\tilde{P}^i \in]-\infty; -0.675P_{ref}] \cup [0.45P_{ref}; +\infty[,$$
$$\text{where} \quad \tilde{P}^i = \frac{1}{\Gamma_i}\sum_j P_j W_{ij} V_j,$$

where $P_{ref} = \frac{1}{2}\rho_0 U_0^2$ is the reference pressure. This enables refining particles around the stagnation point and around the pressure drop on the cylinder side when a vortex is released. To avoid unwanted particle refinement during the initial transient, this criterion is activated only for $tU/D > 2.5\pi$, that is, after the initial imposed motion of the cylinder. The effect of refinement strategy c is depicted in Fig. 22, where the pressure field and the particle size distribution are shown for two time instants $tU_0/d = 97$ and $tU_0/d = 99.5$ characterized by maximum and minimum lift forces, respectively. The area with the finest resolution is not equally distributed around the cylinder: it is established around the stagnation point and deforms following the vortex shedding pattern. Further, comparing the two instants, the finest region is overturned with respect to the $y = 0$ line, as expected since the two instants are in opposite phases.

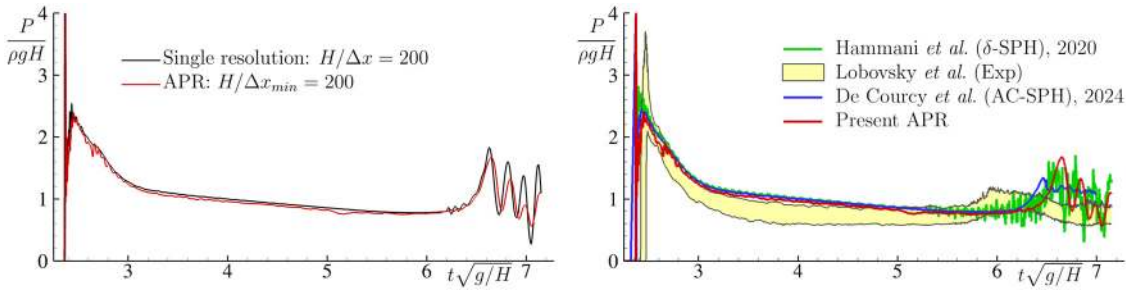

FIG. 20. Inviscid dam-break. Temporal evolution of the pressure at probe P1 located at $y = 0.01H$ on the right vertical wall, compared to single-resolution (left plot) and reference results (right plot). For the experimental results by Lobovský *et al.* the lines encompassing the yellow region correspond to the 2.5% and 97.5% percentile values of the reproducibility investigation.

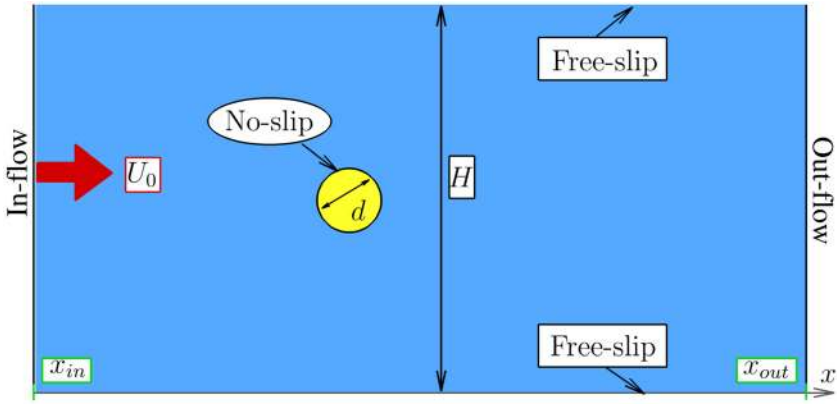

FIG. 21. Flow past a cylinder at $Re = 200$. Sketch of the problem geometry.

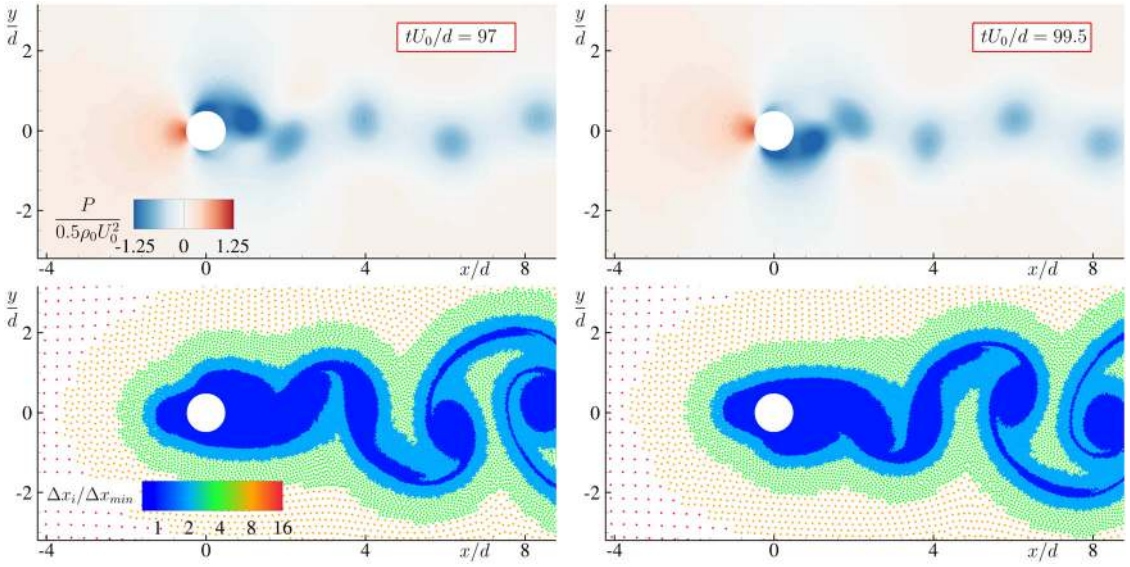

FIG. 22. Flow past a cylinder at $Re = 200$. Pressure field (top) and particle size distribution (bottom) obtained at $tU_0/d = 97$ (left column) and $tU_0/d = 99.5$ (right column) with the present APR when both criteria 4 and 5 are activated, i.e., strategy c, with $\Delta x_{min} = d/50$. In top plots, the particles are displayed with a size proportional to Δx_i.

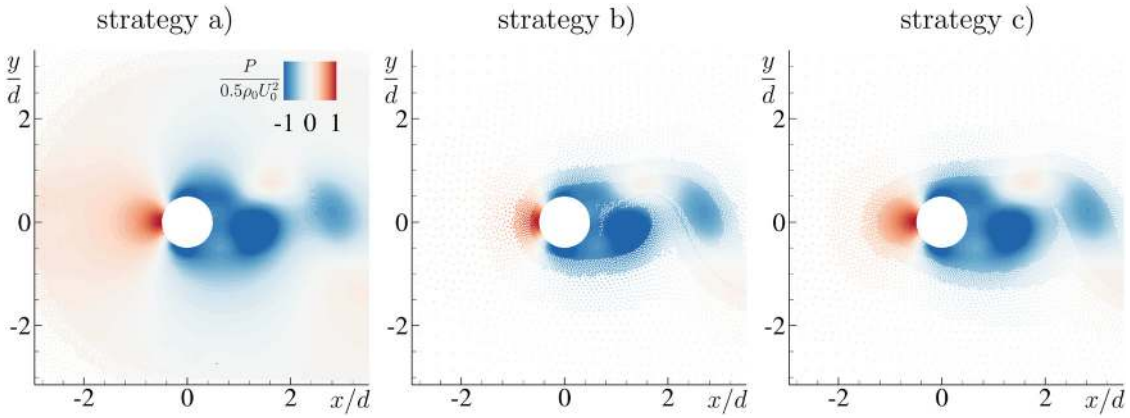

FIG. 23. Flow past a cylinder at $Re = 200$. Pressure field obtained at $tU_0/d = 96$ with $\Delta x_{min} = d/50$. Left: strategy a, i.e., with a geometric box. Center: strategy b, i.e., with criterion 4. Right: strategy c, i.e., with criteria 4 and 5.

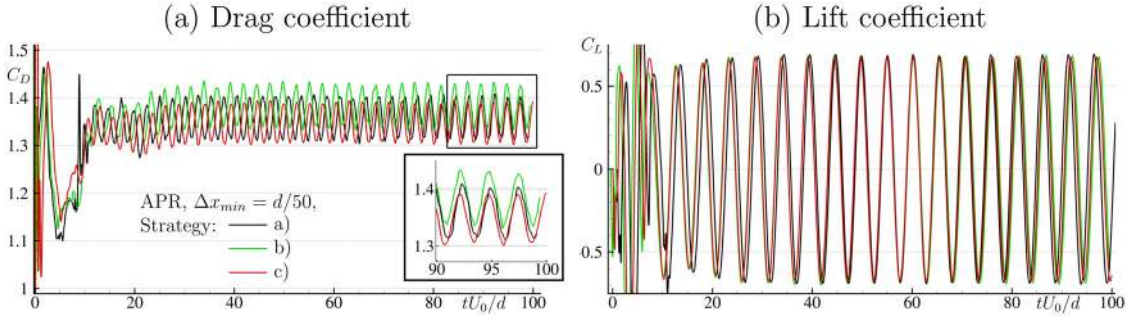

FIG. 24. Flow past a cylinder at $Re = 200$. Temporal evolution of the drag (left plot) and lift (right plot) coefficients obtained with $\Delta x_{min} = d/50$ for the different refinement strategies a–c.

To better highlight the effect of the different criteria considered, Fig. 23 reports a comparison of the pressure field obtained using refinement strategies (a)–(c). The finest particle resolution is the same for the three cases and equal to $\Delta x_{min} = d/50$. A comparison between strategies (b) and (c) shows that the latter results in only a marginal expansion of the region characterized by the finest resolution. Conversely, using strategy (a) the refinement zone largely covers all the flow regions where significant pressure gradients occur and, as mentioned above, can be considered as a fair representation of the single-resolution case.

In Fig. 24, the effect of the different refinement strategies on the forces in terms of drag coefficient $C_D = \frac{F_x}{\frac{1}{2}\rho_0 d U_0^2}$ (left plot) and lift coefficient $C_L = \frac{F_y}{\frac{1}{2}\rho_0 d U_0^2}$, are shown. F_x and F_y are the forces on the cylinder in the horizontal and vertical directions, respectively. The measured forces have been post-processed with a low-pass Butterworth filter with a cut frequency equal to $f_{cut} d/U_0 = 1$. The case using strategy (b) results in an overprediction of about 10% of C_D with respect to the other two cases. Thanks to the small extension of the high-resolution region obtained through criterion 5, strategy (c) provides results similar to those obtained with strategy (a) in terms of drag coefficient. As for the lift force C_L, the three solutions are all in quite good agreement.

Table VIII reports the CPU costs related to the different refinement strategies. Forty-two processors on a workstation equipped with 48 cores Intel(R) Xeon(R) Gold 5220R CPU at 2.20 GHz have been used in all cases. Strategies (b) and (c) are very close, as expected. Conversely, strategy (a) is about three times more expensive than the others. Therefore, only strategy (c) will be considered hereinafter. It is important to underline that this strategy can be applied only if the pressure field is free from numerical noise. Otherwise, spurious particle refinement might occur in regions of little interest.

In Fig. 25, a convergence analysis is reported for both C_D and C_L signals using three different spatial resolutions, namely $\Delta x_{min} = d/25$, $\Delta x_{min} = d/50$, and $\Delta x_{min} = d/75$. The solution can be considered

TABLE VIII. Flow past a cylinder at $Re = 200$. Number of particles and CPU time required for $\Delta x_{min} = d/50$ depending on the refinement criteria used.

Refinement strategy	CPU time	Number of particles
(a) APR with geometric box	8h34 min	≈300 000
(b) APR with criterion 4	3h01 min	≈71 000
(c) APR with criteria 4 and 5	3h11 min	≈91 000

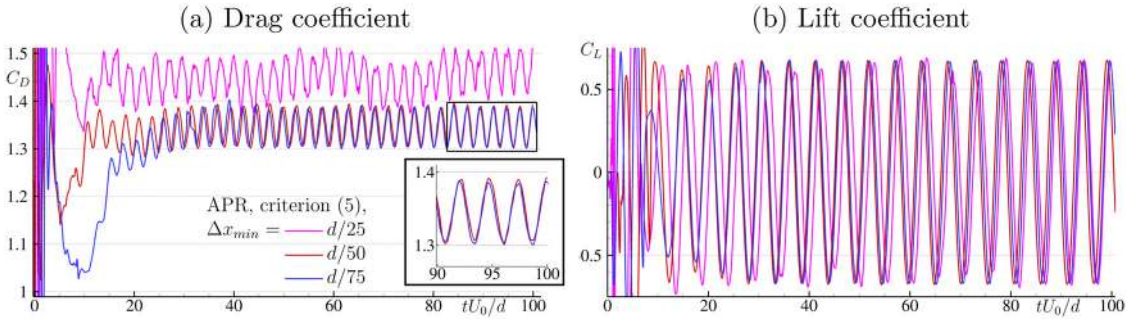

FIG. 25. Flow past a cylinder at $Re = 200$. Temporal evolution of the drag (left plot) and lift (right plot) coefficients obtained with strategy c for three different finest spatial resolutions, namely $\Delta x_{min} = d/25$, $\Delta x_{min} = d/50$, and $\Delta x_{min} = d/75$.

practically converged with $\Delta x_{min} = d/50$ in terms of both amplitude and frequency. By contrast, the resolution $\Delta x_{min} = d/25$ largely overestimates the average value of C_D, whereas the C_L is in good agreement with the other solutions. Therefore, the resolution $\Delta x_{min} = d/50$ is retained in the following and in Sec. VI F.

In Table IX, the obtained results are compared to several reference solutions from the available literature. Results using both weakly compressible and incompressible SPH models are considered as well as solutions from well-established mesh-based methods. Regarding the average value of C_D, a fair agreement is observed with the results from Refs. 44, 49, 61, and 77, whereas a difference of about 10% is observed with respect to Refs. 2 and 10. As for the C_L, errors are below 10% with most of the considered references.

The Strouhal number $\mathrm{St} = fD/U_0$ was computed considering the time window $tU_0/d = [60; 100]$ and is equal to $St = 0.190$ for $\Delta x_{min} = d/50$. This value is in very good agreement with the prediction by Ref. 44, with discrepancies of less than 10% relative to the other references. Finally, in Fig. 26, the vorticity field is reported. The classical von Kármán vortex street is well visible, and no spurious effects are observed even in the zone characterized by large variations of Δx. The right plot presents a zoomed-in view near the cylinder, clearly illustrating that regions of high vorticity are well included within the finest resolution region.

F. Flow past an immersed cylinder below the free surface at *Fr*=1 and *Re*=180

In the present section, a flow past an immersed cylinder below the free surface in an open channel is investigated. This problem was

TABLE IX. Flow past a cylinder at $Re = 200$. Drag and lift coefficients and the Strouhal number obtained with the proposed APR are compared to the results of the literature.

	Spatial resolution	C_D	C_L	St
Liu *et al.*,[44] mesh based	⋯	1.31 ± 0.049	± 0.69	0.192
Calhoun,[10] FVM	$\Delta x = d/20$	1.172 ± 0.058	± 0.668	0.202
Ng *et al.*,[61] mesh based	⋯	1.3730 ± 0.05	± 0.724	⋯
Marrone *et al.*,[49] $\delta-$SPH	$\Delta x = d/100$	1.38 ± 0.05	± 0.68	0.200
Sun *et al.*,[77] δ^+-SPH, APR	$\Delta x_{min} = d/100$	1.345 ± 0.05	± 0.732	⋯
Asai *et al.*,[2] ISPH	$\Delta x = d/80$	1.270 ± 0.046	± 0.659	0.196
Present, APR	$\Delta x_{min} = d/50$	1.345 ± 0.045	± 0.675	0.190

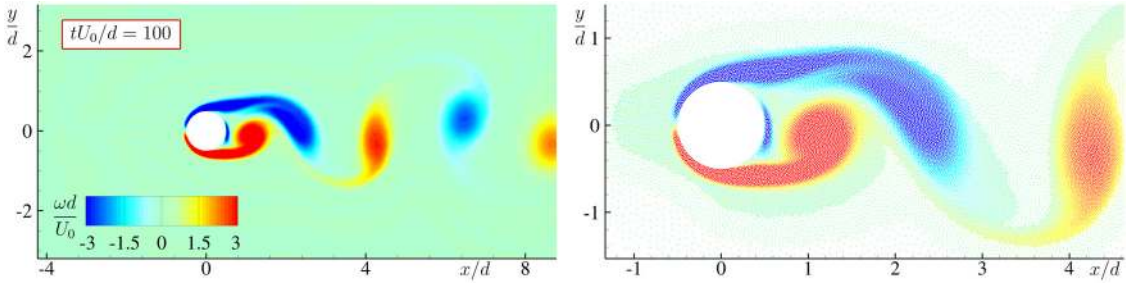

FIG. 26. Flow past a cylinder at $Re = 200$. Vorticity field at $tU_0/d = 100$ obtained with the APR criterion 5 for $\Delta x_{min} = d/50$.

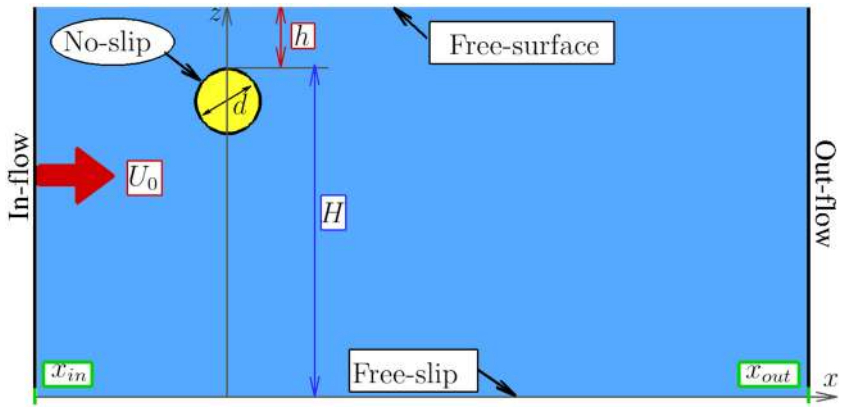

FIG. 27. Flow past an immersed cylinder below the free surface at $Fr = 1$ and $Re = 180$. Sketch of the problem geometry.

first simulated with SPH in Ref. 9 and corresponds to the "Sequence 2" of that article.

Precisely, the Froude and Reynolds numbers are, respectively, set to $Fr = U_0/\sqrt{gd} = 1$ and $Re = \rho_0 U_0 d/\mu = 180$ with U_0 the inflow velocity, g the gravity magnitude, and d the diameter of the cylinder. The ratio between the cylinder immersion and cylinder diameter is $h/d = 1.5$, and the fluid depth is $\frac{H+h}{d} = 6$ as represented in Fig. 27. The reference scales are the length d, the velocity U_0, the time d/U_0, the vorticity U_0/d, the pressure $\frac{1}{2}\rho_0 U_0^2$ and the force $\frac{1}{2}\rho_0 U_0^2 d$. The speed of sound is $c_0 = 10\sqrt{g(h+H)}$. The drag coefficient is defined as $C_D(t) = \frac{F_x(t)}{\frac{1}{2}\rho_0 d U_0^2}$, F_x being the force exerted by the fluid onto the cylinder in the horizontal direction. This test case was also studied in Ref. 12 in order to validate a coupling between the SPH and FV methods. The SPH method was used in a small zone above the cylinder to better capture the free-surface deformation in this zone, whereas the FV method was employed elsewhere. These results, along with those in Ref. 9, are adopted here as reference solutions.

In agreement with the outcomes of Sec. VI E, the minimum spatial resolution is fixed to $\Delta x_{min} = d/50$ with four refinement levels enabled, resulting in a maximum spatial resolution of $\Delta x = d/6.25$. The inflow and outflow limits are positioned vertically at $x_{in}/d = -11$ and $x_{out}/d = 22$, respectively. The spatial resolution for the inflow is managed to be in line with criterion 3, that is, using $\Delta x = d/50$ for $y/d \geq 1.84$, $\Delta x = d/25$ for $y/d \in [1.52; 1.84[$, $\Delta x = d/12.5$ for $y/d \in [0.88; 1.52[$, and $\Delta x = d/6.25$ for $y/d < 0.88$. In order to anticipate the development of the alternate vortex shedding, the same initial motion of the cylinder as in Sec. VI E is applied.

For the considered flow regime, a breaking wave is generated downstream of the cylinder. At each breaking cycle the plunging jet produces a vortical structure. The latter couples with the vortexes in the underlying von Kármán wake generated by the cylinder. In order to capture these phenomena, a fine resolution is needed at the free surface as well as in the boundary layer around the cylinder. Therefore, all criteria 1–5 are activated. Specifically, criterion 3 applies in the free-surface region, and criterion 4 applies close to the cylinder surface (but is disabled on the bottom part of the tank). As for criterion 5 on the dynamic pressure component, the same thresholds apply as in Sec. VI E, that is

$$\tilde{P}^i_{dyn} \in]-\infty; -0.675P_{ref}] \cup [0.45P_{ref}; +\infty[,$$

$$\text{where} \quad \tilde{P}^i_{dyn} = \frac{1}{\Gamma_i}\sum_j \left[P_j - \rho_0 \boldsymbol{g}\cdot(\boldsymbol{x}_j - \boldsymbol{x}_0)\right] W_{ij} V_j,$$

where $\boldsymbol{x}_0$ is the reference position of the free surface. This dynamic refinement is activated in the same manner as in Sec. VI E, i.e., for $tU_0/d > 2.5\pi$.

The left column of Fig. 28 reports the particle size distribution. The features of the local refinement are similar to those of Fig. 23 except for the additional refinement at the free surface. In the right column of Fig. 28, the dynamic pressure field is represented at $tU_0/d = 62.5$. Again, the obtained fields are smooth, even in zones of large variations of Δx. As for the vorticity field, this is compared to reference results by Bouscasse *et al.*[9] (single-resolution SPH) and Chiron *et al.*[12] (coupled SPH–FV solution where SPH is single resolution) in Fig. 29. A very good agreement with both solutions is observed. The vortex patterns are remarkably similar both in terms of vortex localization and magnitude. Notably, small vortices generated from the wave roller and reconnecting with the cylinder wake are captured as in the reference solutions. Small differences are noted, especially close to the free surface, and they are due to the chaotic behavior induced by the breaking of the free surface.

A single-resolution simulation was also conducted for this test case to assess the computational cost savings. The final simulation time was set to $tU_0/d = 80$. The outcomes are very similar to the APR ones but are shown here only in terms of forces for the sake of conciseness. It results that the present APR scheme is around six times faster in the initial stage of the simulation up to $tU_0/d = 20$, as shown in Table X. Then, this gain decreases due to fine particles entrapped in the cylinder wake (we remind that no particle merging is used in the present study). At the end of the simulation at $tU_0/d = 80$, the overall ratio between multi-resolution and single CPU times is around 2.8. For this analysis as well, 42 processors were utilized on a workstation machine equipped with 48 cores Intel(R) Xeon(R) Gold 5220R CPU at 2.20 GHz. Note that the employment of APR is not useful exclusively for CPU costs but also for data storage and post-processing time.

Finally, the temporal evolution of the drag coefficient is compared to reference results in Fig. 30. A fair comparison is obtained

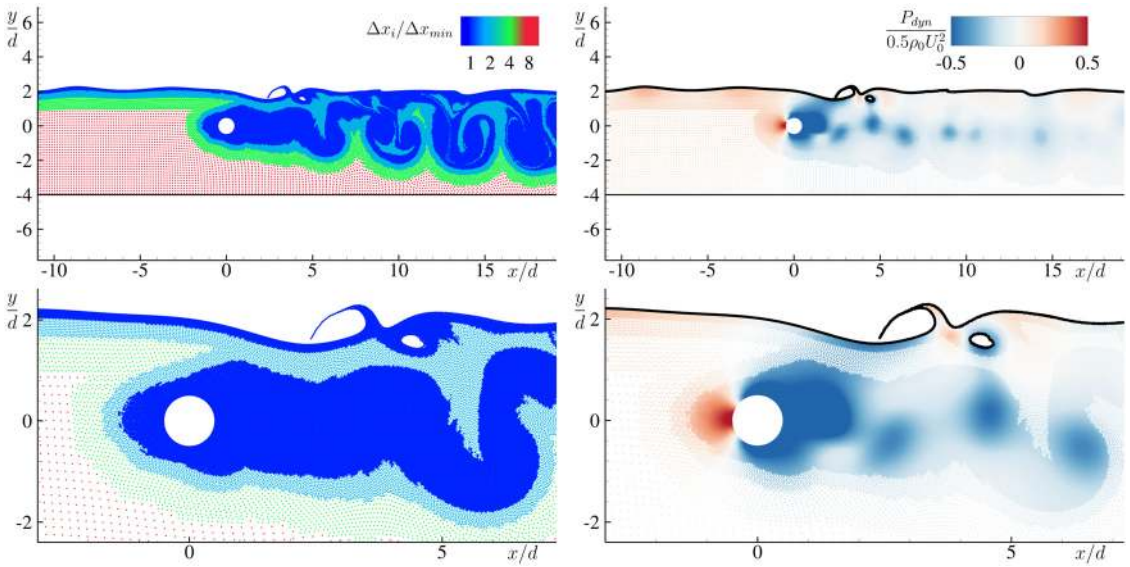

FIG. 28. Flow past an immersed cylinder below the free surface at $Fr = 1$ and $Re = 180$. Left plots: particle size distribution Δx_i. Right plots: dynamic pressure field at $tU_0/d = 62.5$. In the bottom plots, a zoom around the cylinder is provided.

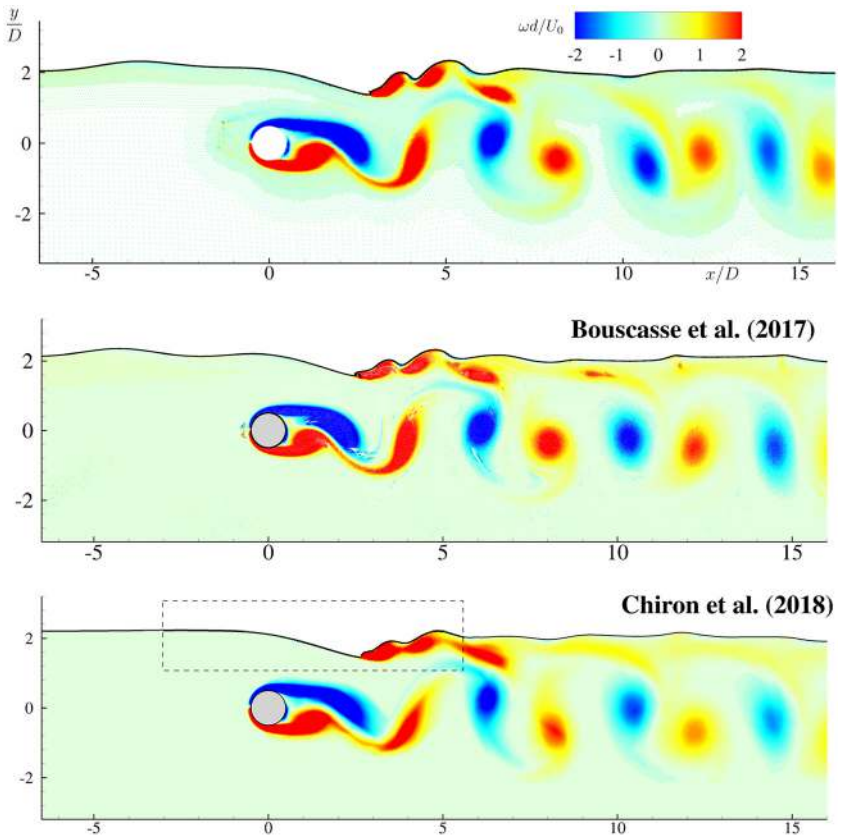

FIG. 29. Flow past an immersed cylinder below the free surface at $Fr = 1$ and $Re = 180$. Vorticity field obtained with APR (top) compared to results by Bouscasse *et al.*[9] (center) and results by Chiron *et al.*[12] (bottom). For the results in Ref. 12, the rectangle in the dashed line represents the SPH zone, whereas FV was used elsewhere. Reproduced with permission from Chiron *et al.*, J. Comput. Phys. **364**, 111–136 (2018). Copyright 2018 Elsevier.

TABLE X. Flow past an immersed cylinder below the free surface at $Fr = 1$ and $Re = 180$. Number of particles and CPU time required at different instants, compared to single-resolution $\Delta x = d/50$.

	$tU_0/d = 20$	$tU_0/d = 40$	$tU_0/d = 80$	$tU_0/d = 110$
Single resolution	498 087 (6.5 h)	498 155 (13.5 h)	498 695 (27.5 h)	...
APR	108 444 (1.2 h)	169 377 (4.0 h)	181 226 (10.4 h 25)	158 212 (15.2 h)

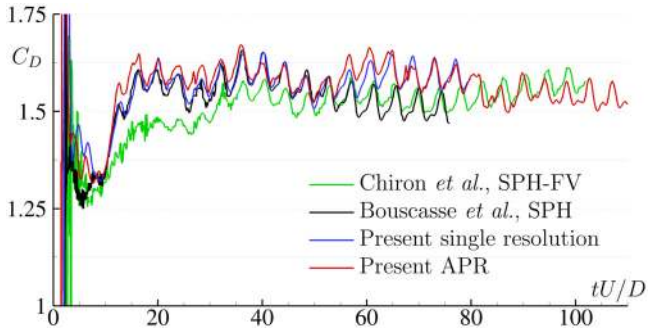

FIG. 30. Flow past an immersed cylinder below the free surface at $Fr = 1$ and $Re = 180$. Temporal evolution of the drag coefficient C_D compared to single resolution and to reference results.

in terms of periods and amplitude of the signals. Low-frequency oscillations are observed in all the solutions, which are due to long waves traveling from the cylinder toward the inlet and locally raising the free surface level above the cylinder. Note that for comparison purposes and since the vortex shedding did not start at the same instant for all the results, a time-shift has been applied to the reference results.

VII. CONCLUSION

In the present work, an in-depth analysis of the existing works about APR in SPH has shown that, in fact, most of the techniques derived in the literature can be categorized into three main approaches. These approaches mainly depend on the selected SPH operators. In particular, the adoption of accurate SPH operators (Approach n.3) allows for large variations of the particle sizes without the need for buffer regions or variable smoothing-length treatments. However, this approach has been restricted to internal flows due to inherent difficulties in treating the free surface with these types of operators. Recently in Ref. 54, the RHOD-SPH scheme has been derived, where accurate but non-conservative operators are employed in the bulk of fluid and conservative ones in the free-surface region. However, this scheme was restricted to single-resolution cases.

Then, in the present work, the RHOD-SPH scheme has been generalized for APR purposes, resulting in an extension of Approach n.3 to free-surface flows. To this end, Riemann-based diffusive terms in the SPH context have been generalized to particles of different sizes. An extension of the PST has also been proposed. Note that these generalizations can also be adopted in the framework of Approach n.1. A splitting procedure has been employed with refinement close to the free surface or to solid boundaries. Thus making the present APR scheme flexible and efficient. Particularly, the choices made here allow for preserving a "gather"-type of implementation, which is particularly effective with GPU accelerators.

The validation has been performed on six different cases. Similar results have been obtained in APR and single resolution even for challenging cases with a significant gain in terms of computational cost, reduction of post-processing time consumption, and data savings, especially compared to APR techniques using buffer regions. The results have also been compared to reference results, showing a good agreement. The resulting formulation is easy to implement and turned out to be robust, at least for 2D test cases. In the proposed test cases, a dynamic refinement criterion based on the pressure field was also tested, demonstrating that the proposed APR approach effectively supports adaptivity driven by flow-dependent fields. In principle, this capability can be readily extended to other flow properties, such as velocity gradients or more complex derived quantities. The development of a suitable particle coalescing procedure and extension to the 3D framework are left to future work.

ACKNOWLEDGMENTS

The research leading to these results was mainly funded by the Siemens Digital Industries Software Chair signed with École Centrale Nantes. This work was also partially funded by the HASTA project (Grant No. 101138003) as part of the European Union Horizon research programme. Views and opinions expressed are, however, those of the authors only and do not necessarily reflect those of the European Union. Neither the European Union nor the granting authority can be held responsible for them. Additionally, the authors thank Dr. Francesco Ricci for his precious help regarding the comparison of the results on the test case of the water entry of a 2D V-shaped body.

AUTHOR DECLARATIONS

Conflict of Interest

The authors have no conflicts to disclose.

Author Contributions

J. Michel: Investigation (lead); Validation (equal); Visualization (equal); Writing – original draft (equal); Writing – review & editing (equal). **G. Oger:** Supervision (equal); Writing – original draft (equal); Writing – review & editing (equal). **D. Le Touzé:** Supervision (equal); Writing – original draft (equal); Writing – review & editing (equal). **A. Colagrossi:** Conceptualization (equal); Supervision (equal); Writing – review & editing (equal). **S. Marrone:** Supervision (equal); Validation

(equal); Writing – original draft (equal); Writing – review & editing (equal).

DATA AVAILABILITY

The data that support the findings of this study are available from the corresponding author upon reasonable request.

APPENDIX: INFLUENCE OF THE $R/\Delta x$ RATIO

In this section, we propose to explore what happens with a ratio $\frac{R}{\Delta x} \neq 4$. Two cases have then to be considered: (i) $\frac{R}{\Delta x} < 4$ and (ii) $\frac{R}{\Delta x} > 4$. In the former case, reducing the kernel support size may result in an insufficient number of coarse neighbors, as illustrated in the left plot of Fig. 31, where only one neighbor particle lies within

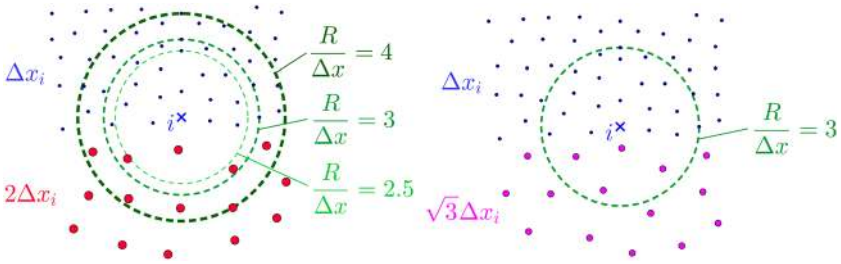

FIG. 31. Different choices of the $R/\Delta x$ ratio: sketches of the particle neighborhood depending on value $\varepsilon_{\Delta x}$. Left: $\varepsilon_{\Delta x} = 2$. Right: $\varepsilon_{\Delta x} = \sqrt{3}$.

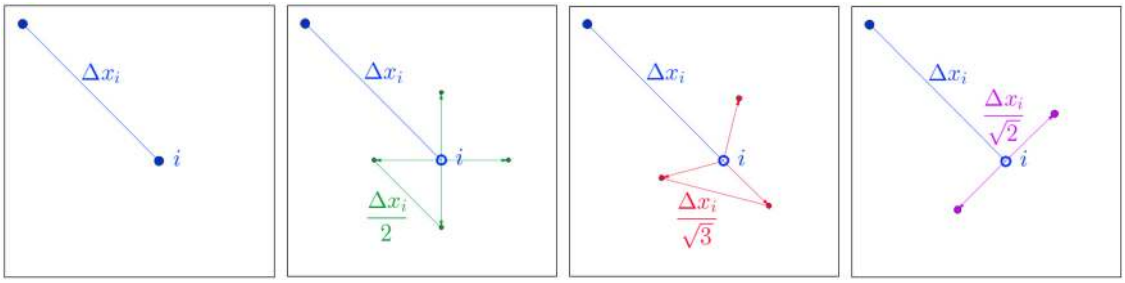

FIG. 32. Sketches of the different particle-splitting patterns and corresponding $\varepsilon_{\Delta x}$. First plot: before splitting; second plot: square splitting; third plot: triangular splitting; and fourth plot: dichotomic splitting.

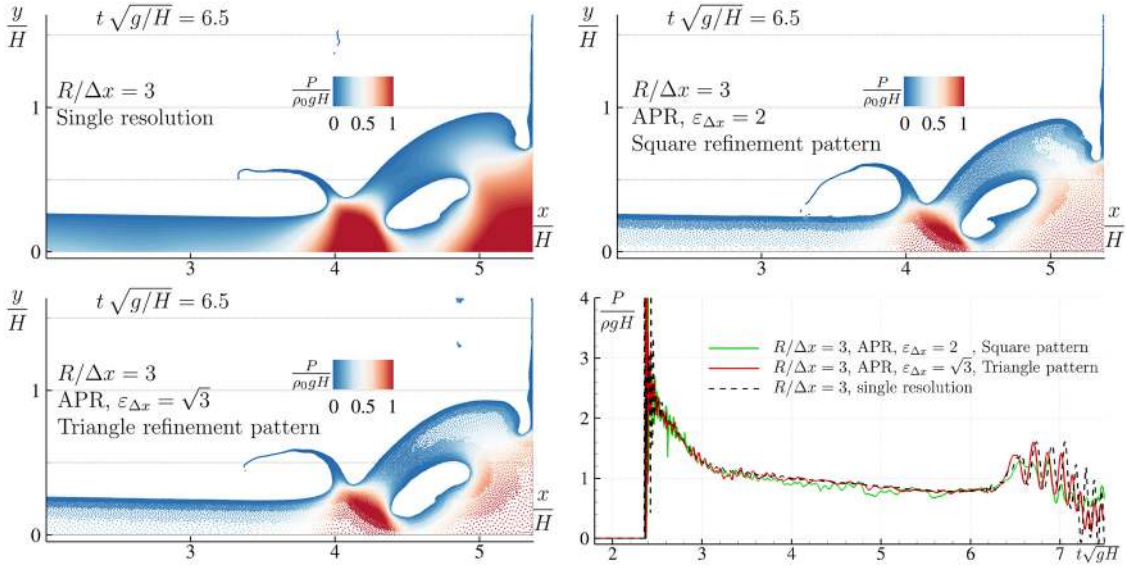

FIG. 33. The dam-break test case as described in Sec. VI D simulated with $R/\Delta x = 3$: comparison of the single-resolution result (top left) with the APR solution with $\varepsilon_{\Delta x} = 2$ (top right) and with $\varepsilon_{\Delta x} = \sqrt{3}$ (bottom left). The bottom-right plot reports the comparison of the pressure signals at probe P1.

the kernel support of a fine particle with $\frac{R}{\Delta x} = 2.5$. In contrast, in the case $\frac{R}{\Delta x} > 4$ the kernel support is sufficiently large to encompass multiple coarse neighbors, preventing this issue.

In order to use smaller values of $R/\Delta x$, it is possible to change the ratio $\varepsilon_{\Delta x} = \frac{\Delta x_{l+1}}{\Delta x_l}$, that is, the ratio between the particle sizes of two adjacent refinement levels ($l = 1$ corresponds to the minimum particle size adopted). For example, in the right plot of Fig. 31, a sketch of the particle distribution and of the kernel support is reported for $\frac{R}{\Delta x} = 3$ and $\varepsilon_{\Delta x} = \sqrt{3}$. In this case, a larger number of coarse neighbors is present. The influence of this choice is tested in the following.

It is important to note that changing $\varepsilon_{\Delta x}$ implies also changing the refinement pattern. Indeed, the chosen $\varepsilon_{\Delta x}$ shall be consistent with the adopted refinement pattern to ensure conservation of the geometrical volume during the splitting procedure. More specifically, if a coarse particle is divided into N_{split} child particles of equal volume, the size ratio between the two resolution levels becomes $\varepsilon_{\Delta x} = \sqrt{N_{split}}$. In Fig. 32, the splitting patterns and corresponding $\varepsilon_{\Delta x}$ values are reported for $N_{split} = [4, 3, 2]$.

The same principle applies when using larger $R/\Delta x$ ratios: the greater number of coarse neighbors in this case permits higher values of $\varepsilon_{\Delta x}$, enabling larger variations in particle resolution. Note that for values of $N_{split} \neq 4$, the equations in Sec. V A must be modified consistently.

In Fig. 33, the influence of $R/\Delta x$ is studied on the dam-break test case described in Sec. VI D. The solution obtained with single resolution and $R/\Delta x = 3$ is compared to the APR counterpart with $\varepsilon_{\Delta x} = 2$ (square pattern) and $\varepsilon_{\Delta x} = \sqrt{3}$ (triangular pattern). No substantial differences among the three cases are observed in terms of flow evolution. However, the comparison of the pressure signals (bottom-right plot of Fig. 33) indicates that the triangular pattern exhibits a lower level of noise and a closer agreement with the single-resolution result. This confirms that the adoption of smaller $R/\Delta x$ ratios are more effective when combined with smaller values of $\varepsilon_{\Delta x}$.

REFERENCES

[1]Antuono M., Sun P. N., Marrone S., and Colagrossi A., "The δ-ALE-SPH model: An arbitrary Lagrangian-Eulerian framework for the δ-SPH model with particle shifting technique," Comput. Fluids **216**, 104806 (2021).

[2]Asai M., Fujioka S., Saeki Y., Morikawa D. S., and Tsuji K., "A class of second-derivatives in the smoothed particle hydrodynamics with 2nd-order accuracy and its application to incompressible flow simulations," Comput. Methods Appl. Mech. Eng. **415**, 116203 (2023).

[3]Barcarolo D. A., Le Touzé D., Oger G., and de Vuyst F., "Adaptive particle refinement and derefinement applied to the smoothed particle hydrodynamics method," J. Comput. Phys. **273**, 640–657 (2014).

[4]Bate M. R., Bonnell I. A., and Price N. M., "Modelling accretion in protobinary systems," Mon. Not. R. Astron. Soc. **277**(2), 362–376 (1995).

[5]Berger M. J. and Oliger J., "Adaptive mesh refinement for hyperbolic partial differential equations," J. Comput. Phys. **53**(3), 484–512 (1984).

[6]Bian X., Li Z., and Karniadakis G. E., "Multi-resolution flow simulations by smoothed particle hydrodynamics via domain decomposition," J. Comput. Phys. **297**, 132–155 (2015).

[7]Bonet J. and Lok T. S. L., "Variational and momentum preservation aspects of smoothed particle hydrodynamics formulations," Comput. Methods Appl. Mech. Eng. **180**, 97–115 (1999).

[8]Bouscasse B., Colagrossi A., Marrone S., and Antuono M., "Nonlinear water wave interaction with floating bodies in SPH," J. Fluids Struct. **42**, 112–129 (2013).

[9]Bouscasse B., Colagrossi A., Marrone S., and Souto-Iglesias A., "SPH modelling of viscous flow past a circular cylinder interacting with a free surface," Comput. Fluids **146**, 190–212 (2017).

[10]Calhoun D., "A Cartesian grid method for solving the two-dimensional streamfunction-vorticity equations in irregular regions," J. Comput. Phys. **176**(2), 231–275 (2002).

[11]Chen D., Huang W., Huang D., and Liang C., "An adaptive multi-resolution SPH approach for three-dimensional free-surface flow with fluid impacting," Eng. Anal. Boundary Elem. **155**, 642–651 (2023).

[12]Chiron L., Marrone S., Di Mascio A., and Le Touzé D., "Coupled SPH–FV method with net vorticity and mass transfer," J. Comput. Phys. **364**, 111–136 (2018).

[13]Chiron L., Oger G., De Leffe M., and Le Touzé D., "Analysis and improvements of adaptive particle refinement (APR) through CPU time, accuracy and robustness considerations," J. Comput. Phys. **354**, 552–575 (2018).

[14]Colagrossi A., "A meshless Lagrangian method for free-surface and interface flows with fragmentation," Ph.D. thesis (Università di Roma La Sapienza, 2005).

[15]Colagrossi A., Antuono M., and Le Touzé D., "Theoretical considerations on the free-surface role in the smoothed-particle-hydrodynamics model," Phys. Rev. E **79**(5), 056701 (2009).

[16]Colagrossi A., Bouscasse B., Antuono M., and Marrone S., "Particle packing algorithm for SPH schemes," Comput. Phys. Commun. **183**(2), 1641–1683 (2012).

[17]Colagrossi A. and Landrini M., "Numerical simulation of interfacial flows by smoothed particle hydrodynamics," J. Comput. Phys. **191**, 448–475 (2003).

[18]De Courcy J. J., Rendall T. C. S., Constantin L., Titurus B., and Cooper J. E., "Incompressible δ-SPH via artificial compressibility," Comput. Methods Appl. Mech. Eng. **420**, 116700 (2024).

[19]De Zeeuw D. and Powell K. G., "An adaptively-refined Cartesian mesh solver for the Euler equations," J. Comput. Phys. **101**(2), 453–454 (1992).

[20]Dilts G. A., "Moving-least-squares-particle hydrodynamics—I. Consistency and stability," Int. J. Numer. Methods Eng. **44**(8), 1115–1155 (1999).

[21]Domínguez J. M., Crespo A. J. C., and Gómez-Gesteira M., "Optimization strategies for CPU and GPU implementations of a smoothed particle hydrodynamics method," Comput. Phys. Commun. **184**(3), 617–627 (2013).

[22]Feldman J. and Bonet J., "Dynamic refinement and boundary contact forces in SPH with applications in fluid flow problems," Int. J. Numer. Methods Eng. **72**(3), 295–324 (2007).

[23]Gao T., Qiu H., and Fu L., "A block-based adaptive particle refinement SPH method for fluid–structure interaction problems," Comput. Methods Appl. Mech. Eng. **399**, 115356 (2022).

[24]Gotoh H. and Khayyer A., "On the state-of-the-art of particle methods for coastal and ocean engineering," Coastal Eng. J. **60**(1), 79–103 (2018).

[25]Haftu A., Muta A., and Ramachandran P., "Parallel adaptive weakly-compressible SPH for complex moving geometries," Comput. Phys. Commun. **277**, 108377 (2022).

[26]Hammani I., Marrone S., Colagrossi A., Oger G., and Le Touzé D., "Detailed study on the extension of the δ-SPH model to multi-phase flow," Comput. Methods Appl. Mech. Eng. **368**, 113189 (2020).

[27]Hermange C., Oger G., Le Chenadec Y., and Le Touzé D., "A 3D SPH–FE coupling for FSI problems and its application to tire hydroplaning simulations on rough ground," Comput. Methods Appl. Mech. Eng. **355**, 558–590 (2019).

[28]Hernquist L. and Katz N., "TreeSPH: A unification of SPH with the hierarchical tree method," Astrophys. J., Suppl. Ser. **70**, 419–446 (1989).

[29]Hong Y., Yang X., Liu K., Wu Y., and Wu Y., "Adaptive resolution SPH method for non-Newtonian slurry mixing," Int. J. Mech. Sci. **289**, 110053 (2025).

[30]Hu W., Pan W., Rakhsha M., Tian Q., Hu H., and Negrut D., "A consistent multi-resolution smoothed particle hydrodynamics method," Comput. Methods Appl. Mech. Eng. **324**, 278–299 (2017).

[31]Janodet R., Guillamón C., Moureau V., Mercier R., Lartigue G., Bénard P., Ménard T., and Berlemont A., "A massively parallel accurate conservative level set algorithm for simulating turbulent atomization on adaptive unstructured grids," J. Comput. Phys. **458**, 111075 (2022).

[32]Khayyer A., Gotoh H., and Shimizu Y., "Comparative study on accuracy and conservation properties of two particle regularization schemes and proposal of an optimized particle shifting scheme in ISPH context," J. Comput. Phys. **332**, 236–256 (2017).

[33]Khayyer A., Shimizu Y., Gotoh H., and Hattori S., "Multi-resolution ISPH-SPH for accurate and efficient simulation of hydroelastic fluid-structure interactions in ocean engineering," Ocean Eng. **226**, 108652 (2021).
[34]Khayyer A., Tsuruta N., Shimizu Y., and Gotoh H., "Multi-resolution MPS for incompressible fluid-elastic structure interactions in ocean engineering," Appl. Ocean Res. **82**, 397–414 (2019).
[35]Khorasanizade S. and Sousa J. M. M., "An adaptive fully-Lagrangian meshless method for incompressible laminar flow airfoil studies," Aerosp. Sci. Technol. **64**, 161–170 (2017).
[36]Kitsionas S. and Whitworth A. P., "Smoothed particle hydrodynamics with particle splitting, applied to self-gravitating collapse," Mon. Not. R. Astron. Soc. **330**(1), 129–136 (2002).
[37]Lastiwka M., Quinlan N., and Basa M., "Adaptive particle distribution for smoothed particle hydrodynamics," Int. J. Numer. Methods Fluids **47**(10–11), 1403–1409 (2005).
[38]Le Touzé D., Colagrossi A., Colicchio G., and Greco M., "A critical investigation of smoothed particle hydrodynamics applied to problems with free-surfaces," Int. J. Numer. Methods Fluids **73**(7), 660–691 (2013).
[39]Le Touzé D. and Colagrossi A., "Smoothed particle hydrodynamics for free-surface and multiphase flows: A review," Rep. Prog. Phys. **88**, 037001 (2025).
[40]Lekkala M. R., Latheef M., Jung J. H., Coraddu A., Zhu H., Srinil N., Lee B.-H., and Kim D. K., "Recent advances in understanding the flow over bluff bodies with different geometries at moderate Reynolds numbers," Ocean Eng. **261**, 111611 (2022).
[41]Liang C., Huang W., and Chen D., "A pressure-dependent adaptive resolution scheme for smoothed particle hydrodynamics simulation of underwater explosion," Ocean Eng. **270**, 113695 (2023).
[42]Libersky L. D., Petschek A. G., Carney T. C., Hipp J. R., and Allahdadi F. A., "High strain Lagrangian hydrodynamics a three-dimensional SPH code for dynamic material response," J. Comput. Phys. **109**(1), 67–75 (1993).
[43]Lind S. J., Xu R., Stansby P. K., and Rogers B. D., "Incompressible smoothed particle hydrodynamics for free-surface flows: A generalised diffusion-based algorithm for stability and validations for impulsive flows and propagating waves," J. Comput. Phys. **231**(4), 1499–1523 (2012).
[44]Liu C., Zheng X., and Sung C. H., "Preconditioned multigrid methods for unsteady incompressible flows," J. Comput. Phys. **139**(1), 35–57 (1998).
[45]Liu X. and Zhang S., "Development of adaptive multi-resolution MPS method for multiphase flow simulation," Comput. Methods Appl. Mech. Eng. **387**, 114184 (2021).
[46]Lobovský L., Botia-Vera E., Castellana F., Mas-Soler J., and Souto-Iglesias A., "Experimental investigation of dynamic pressure loads during dam break," J. Fluids Struct. **48**, 407–434 (2014).
[47]Lyu H.-G., Sun P.-N., Miao J.-M., and Zhang A.-M., "3D multi-resolution SPH modeling of the water entry dynamics of free-fall lifeboats," Ocean Eng. **257**, 111648 (2022).
[48]Löhner R., "An adaptive finite element scheme for transient problems in CFD," Comput. Methods Appl. Mech. Eng. **61**(3), 323–338 (1987).
[49]Marrone S., Colagrossi A., Antuono M., Colicchio G., and Graziani G., "An accurate SPH modeling of viscous flows around bodies at low and moderate Reynolds numbers," J. Comput. Phys. **245**, 456–475 (2013).
[50]Marrone S., Colagrossi A., Park J. S., and Campana E. F., "Challenges on the numerical prediction of slamming loads on LNG tank insulation panels," Ocean Eng. **141**, 512–530 (2017).
[51]Marrone S., Colagrossi A., Le Touzé D., and Graziani G., "Fast free-surface detection and level-set function definition in SPH solvers," J. Comput. Phys. **229**(10), 3652–3663 (2010).
[52]McLoone M. and Quinlan N. J., "Particle transport velocity correction for the finite volume particle method for multi-resolution particle distributions and exact geometric boundaries," Eng. Anal. Boundary Elem. **114**, 114–126 (2020).
[53]Michel J., Antuono M., Oger G., and Marrone S., "Energy balance in quasi-Lagrangian Riemann-based SPH schemes," Comput. Methods Appl. Mech. Eng. **410**, 116015 (2023).
[54]Michel J., Colagrossi A., Antuono M., and Marrone S., "A regularized high-order diffusive smoothed particle hydrodynamics scheme without tensile instability," Phys. Fluids **35**(10), 103604 (2023).
[55]Michel J., Vergnaud A., Oger G., Hermange C., and Le Touzé D., "On Particle Shifting Techniques (PSTs): Analysis of existing laws and proposition of a convergent and multi-invariant law," J. Comput. Phys. **459**, 110999 (2022).
[56]Mokos A., Rogers B. D., and Stansby P. K., "A multi-phase particle shifting algorithm for SPH simulations of violent hydrodynamics with a large number of particles," J. Hydraul. Res. **55**(2), 143–162 (2017).
[57]Monaghan J. J. and Gingold R. A., "Shock simulation by the particle method SPH," J. Comput. Phys. **52**(2), 374–389 (1983).
[58]Murante G., Borgani S., Brunino R., and Cha S.-H., "Hydrodynamic simulations with the Godunov smoothed particle hydrodynamics," Mon. Not. R. Astron. Soc. **417**(1), 136–153 (2011).
[59]Muta A. and Ramachandran P., "Efficient and accurate adaptive resolution for weakly-compressible SPH," Comput. Methods Appl. Mech. Eng. **395**, 115019 (2022).
[60]Nelson R. P. and Papaloizou J. C. B., "Variable smoothing lengths and energy conservation in smoothed particle hydrodynamics," Mon. Not. R. Astron. Soc. **270**(1), 1–20 (1994).
[61]Ng Y. T., Min C., and Gibou F., "An efficient fluid–solid coupling algorithm for single-phase flows," J. Comput. Phys. **228**(23), 8807–8829 (2009).
[62]Oger G., Doring M., Alessandrini B., and Ferrant P., "Two-dimensional SPH simulations of wedge water entries," J. Comput. Phys. **213**(2), 803–822 (2006).
[63]Oger G., Marrone S., Le Touzé D., and De Leffe M., "SPH accuracy improvement through the combination of a quasi-Lagrangian shifting transport velocity and consistent ALE formalisms," J. Comput. Phys. **313**, 76–98 (2016).
[64]Omidvar P., Stansby P. K., and Rogers B. D., "Wave body interaction in 2D using smoothed particle hydrodynamics (SPH) with variable particle mass," Int. J. Numer. Methods Fluids **68**(6), 686–705 (2012).
[65]Parshikov A. N. and Medin S. A., "Smoothed particle hydrodynamics using interparticle contact algorithms," J. Comput. Phys. **180**, 358–382 (2002).
[66]Qian Z., Wang L., Zhang C., Zhong Z., and Chen Q., "Conservation and accuracy studies of the LESCM for incompressible fluids," J. Comput. Phys. **489**, 112269 (2023).
[67]Quinlan N. J., Lastiwka M., and Basa M., "Truncation error in mesh-free particle methods," Int. J. Numer. Methods Eng. **66**(13), 2064–2085 (2006).
[68]Randles P. W. and Libersky L. D., "Normalized SPH with stress points," Int. J. Numer. Methods Eng. **48**(10), 1445–1462 (2000).
[69]Reyes López Y., Roose D., and Morfa C. R., "Dynamic particle refinement in SPH: Application to free surface flow and non-cohesive soil simulations," Comput. Mech. **51**, 731–741 (2013).
[70]Ricci F., Vacondio R., Domínguez J. M., and Tafuni A., "Three-dimensional variable resolution for multi-scale modeling in smoothed particle hydrodynamics," Comput. Phys. Commun. **313**, 109609 (2025).
[71]Ricci F., Vacondio R., and Tafuni A., "Multiscale smoothed particle hydrodynamics based on a domain-decomposition strategy," Comput. Methods Appl. Mech. Eng. **418**, 116500 (2024).
[72]Rompteaux A. and Vila J. P., "Calcul du tossage avec 'smart fluids', un code de calcul particulaire compressible," in *7e Journées de l'Hydrodynamique* (SHF, 1999), pp. 165–177.
[73]Shadloo M. S., Oger G., and Le Touzé D., "Smoothed particle hydrodynamics method for fluid flows, towards industrial applications: Motivations, current state, and challenges," Comput. Fluids **136**, 11–34 (2016).
[74]Shibata K., Koshizuka S., Matsunaga T., and Masaie I., "The overlapping particle technique for multi-resolution simulation of particle methods," Comput. Methods Appl. Mech. Eng. **325**, 434–462 (2017).
[75]Spreng F., Vacondio R., Eberhard P., and Williams J. R., "An advanced study on discretization-error-based adaptivity in smoothed particle hydrodynamics," Comput. Fluids **198**, 104388 (2020).
[76]Sun P.-N., Le Touzé D., Oger G., and Zhang A.-M., "An accurate SPH volume adaptive scheme for modeling strongly-compressible multiphase flows. Part 1: Numerical scheme and validations with basic 1D and 2D benchmarks," J. Comput. Phys. **426**, 109937 (2021).
[77]Sun P. N., Colagrossi A., Le Touzé D., and Zhang A.-M., "Extension of the δ-plus-SPH model for simulating vortex-induced-vibration problems," J. Fluids Struct. **90**, 19–42 (2019).
[78]Sun P. N., Colagrossi A., Marrone S., Antuono M., and Zhang A. M., "Multi-resolution Delta-plus-SPH with tensile instability control: Towards high Reynolds number flows," Comput. Phys. Commun. **224**, 63–80 (2018).

[79]Sun P. N., Colagrossi A., Marrone S., Antuono M., and Zhang A. M., "A consistent approach to particle shifting in the δ-plus-SPH model," Comput. Methods Appl. Mech. Eng. **348**, 912–934 (2019).
[80]Sun P. N., Colagrossi A., Marrone S., and Zhang A. M., "The δplus-SPH model: Simple procedures for a further improvement of the SPH scheme," Comput. Methods Appl. Mech. Eng. **315**, 25–49 (2017).
[81]Sun P. N., Pilloton C., Antuono M., and Colagrossi A., "Inclusion of an acoustic damper term in weakly-compressible SPH models," J. Comput. Phys. **483**, 112056 (2023).
[82]Tanaka M., Cardoso R., and Bahai H., "Multi-resolution MPS method," J. Comput. Phys. **359**, 106–136 (2018).
[83]Toro E. F., *Riemann Solvers and Numerical Methods for Fluid Dynamics: A Practical Introduction* (Springer Science & Business Media, 2013).
[84]Vacondio R., Altomare C., De Leffe M., Hu X., Le Touzé D., Lind S., Marongiu J. C., Marrone S., Rogers B. D., and Souto-Iglesias A., "Grand challenges for smoothed particle hydrodynamics numerical schemes," Comput. Part. Mech. **8**, 575–588 (2021).
[85]Vacondio R., Rogers B. D., Stansby P. K., Mignosa P., and Feldman J., "Variable resolution for SPH: A dynamic particle coalescing and splitting scheme," Comput. Methods Appl. Mech. Eng. **256**, 132–148 (2013).
[86]Vacondio R., Rogers B. D., Stansby P. K., and Mignosa P., "Variable resolution for SPH in three dimensions: Towards optimal splitting and coalescing for dynamic adaptivity," Comput. Methods Appl. Mech. Eng. **300**, 442–460 (2016).
[87]Van Leer B., "Towards the ultimate conservative difference scheme. V. A second-order sequel to Godunov's method," J. Comput. Phys. **32**(1), 101–136 (1979).
[88]Vila J.-P., "On particle weighted methods and smooth particle hydrodynamics," Math. Models Methods Appl. Sci. **9**(2), 161–209 (1999).
[89]Violeau D. and Rogers B. D., "Smoothed particle hydrodynamics (SPH) for free-surface flows: Past, present and future," J. Hydraul. Res. **54**(1), 1–26 (2016).
[90]Wackers J., Deng G., Leroyer A., Queutey P., and Visonneau M., "Adaptive grid refinement for hydrodynamic flows," Comput. Fluids **55**, 85–100 (2012).
[91]Wang P.-P., Meng Z.-F., Zhang A.-M., Ming F.-R., and Sun P.-N., "Improved particle shifting technology and optimized free-surface detection method for free-surface flows in smoothed particle hydrodynamics," Comput. Methods Appl. Mech. Eng. **357**, 112580 (2019).
[92]Wendland H., "Piecewise polynomial, positive definite and compactly supported radial functions of minimal degree," Adv. Comput. Math. **4**(4), 389–396 (1995).
[93]Yang Q., Xu F., Yang Y., Dai Z., and Wang J., "A GPU-accelerated adaptive particle refinement for multi-phase flow and fluid-structure coupling SPH," Ocean Eng. **279**, 114514 (2023).
[94]Yang Q., Xu F., Yang Y., and Wang L., "A multi-phase SPH model based on Riemann solvers for simulation of jet breakup," Eng. Anal. Boundary Elem. **111**, 134–147 (2020).
[95]Yang X., Feng S., Wu J., Zhang G., Liang G., and Zhang Z., "Study of the water entry and exit problems by coupling the APR and PST within SPH," Appl. Ocean Res. **139**, 103712 (2023).
[96]Yang X. and Kong S.-C., "Adaptive resolution for multiphase smoothed particle hydrodynamics," Comput. Phys. Commun. **239**, 112–125 (2019).
[97]Yang X., Kong S.-C., Liu M., and Liu Q., "Smoothed particle hydrodynamics with adaptive spatial resolution (SPH-ASR) for free surface flows," J. Comput. Phys. **443**, 110539 (2021).
[98]Zhang C., Rezavand M., and Hu X., "A multi-resolution SPH method for fluid-structure interactions," J. Comput. Phys. **429**, 110028 (2021).
[99]Zhang S., Fan Y., Ren Y., Qian B., and Hu X. Y., "Generalized and high-efficiency arbitrary-positioned buffer for smoothed particle hydrodynamics," Phys. Fluids **36**(12), 127107 (2024).
[100]Zhao R., Faltinsen O., and Aarsnes J., "Water entry of arbitrary two-dimensional sections with and without flow separation," in *21st Symposium on Naval Hydrodynamics* (National Academy Press, Washington, DC, 1996), pp. 408–423.
[101]Zhao Z.-X., Liu H., and Gong Z.-X., "A high-efficiency smoothed particle hydrodynamics model with multi-cell linked list and adaptive particle refinement for two-phase flows," Phys. Fluids **33**(6), 064102 (2021).